CHALMERS
UNIVERSITY OF TECHNOLOGY

New scan strategy for Electron Beam Melting
Process window and microstructure evolution

Master's Thesis in the Master's Programme Materials Engineering

ISMAIL SHOJAI

Department of Industrial and Material Science
Division of Materials and Manufacture
Surface and Microstructure Engineering
CHALMERS UNIVERSITY OF TECHNOLOGY
Gothenburg, Sweden 2019
Master's Thesis 2019

MASTER'S THESIS 2019

New scan strategy for Electron Beam Melting

Process window and microstructure evolution

Master's Thesis in the Master's Programme Materials Engineering

ISMAIL SHOJAI

CHALMERS
UNIVERSITY OF TECHNOLOGY

Department of Industrial and Materials Science
Division of Materials and Manufacture
Surface and Microstructure Engineering
CHALMERS UNIVERSITY OF TECHNOLOGY
Gothenburg, Sweden 2019

New scan strategy for Electron Beam Melting
Process window and microstructure evolution
Master's Thesis in the Master's Programme Materials Engineering

ISMAIL SHOJAI

Examensarbete 2019/ Institutionen för industri- och materialvetenskap,
Chalmers tekniska högskola 2019

Department of Industrial and Materials Science
Division of Materials and Manufacture
Surface and Microstructure Engineering
Chalmers University of Technology
SE-412 96 Gothenburg
Sweden
Telephone: + 46 (0)31-772 1000

Cover:
Optical micrograph showing grain structure and less textured structure along the build direction.
Department of Industrial and Materials Science, Gothenburg, Sweden, 2019

New scan strategy of Electron Beam Melting

Process window and microstructure evolution

Master's thesis in the Master's Programme Materials Engineering

ISMAIL SHOJAI
Department of Industrial and Materials Science
Division of Materials and Manufacture
Surface and Microstructure Engineering
Chalmers University of Technology

ABSTRACT

For the Electron Beam Melting Process, point melt scan strategy is evaluated instead of using a traditional hatch scan strategy. The effect on porosity, microstructure and basic mechanical properties are investigated using TiAl6V4 alloy powder. Different builds with different parameters (spot time, point distance and beam current) are the basis for this work with the objective generating a process window for dense and crack-free specimens. Porosity was characterized based on optical microscope imaging. The occurrence of a new morphology of porosity which was not observed in traditional melting strategies, was investigated more in detail. Especially the relation between spot time and volume energy was analyzed more in detail. Specimens showing a relative density >99.8% were categorized as dense according to threshold set for this work and were therefore basis for further characterization. Thus, microstructural features were investigated using OM on etched specimens and illustrated by correlating different point distances, volume energies, point energies and spot times. In addition, complementary Hardness tests were performed to gain a basic understanding of the mechanical properties of the produced specimens. As a main result of this thesis, a process window for an EBM point melt strategy is proposed leading to dense specimens showing possibility to tailor the microstructure for desired applications respectively.

Key words: EBM, point melt, Hatch scanning strategy, point distance, spot time, scan strategy, microstructures, porosity, BIP, melt pool, Widmanstätten structure, Basketweave structure.

“All's well that ends better.”

—J.R.R. Tolkien

Acknowledgements

Process parameters and effect on microstructural evolution in Electron Beam Melted Ti64 was investigated. All tests have been performed from January 2019 to June 2019 in a collaboration project between Chalmers University of Technology and Arcam EBM. This master's thesis is part of CAM2 collaboration 2019.

The EBM specimens for this thesis were produced and provided by Arcam EBM. Tests and experiments were carried out mostly at Department of Industrial and Material Science. Some experiments were carried out at Arcam Materials Lab.

I would take the opportunity to thank the team at Arcam including Dr Markus Ramsperger and Dr Anders Snis for the help in this thesis.

I would also like to thank Prof Uta Klement, my supervisor and examiner at Chalmers. Special thanks to Prof Eduard Hryha for his contribution during the thesis.

Research engineer Dr Yiming Yao, PhD student Hans Gruber, Dr. Dinesh Mallipeddi and Martin Plomgren at Arcam EBM are thanked for their help and assistance with laboratory equipment and theoretical discussions.

I would also say that all the work and testing in the lab could not be conducted had it not been for the professional help lab instructors and PhD students at the department.

I would also take the time and appreciate my other classmates past and present!

Special thanks to my great friends Fredrik, Erika, Bharat, Johanna, Angelica, Daniel and Alexander during this past five months for helping me whenever needed!

Finally, I must express my very profound gratitude to my mother and to my sister for providing me with unfailing support and continuous encouragement throughout my years of study and through the process of researching and writing this thesis. This accomplishment would not have been possible without them. Thank you.

Gothenburg June 2019

Ismail Shojai

Abbreviations

BCC = Body cantered cubic

HCP = Hexagonal close packed

EBM = Electron Beam Melting

ST = Spot time

PD = Point distance

VE = Volume energy

PE = Point energy

AM = Additive manufacturing

BIP = Beam induced porosity

TAP = Total amount of porosity

LOM = Light optical microscope

Contents

1 Introduction

1.1.1 Background

Currently, Arcam is using a raster line hatch strategy in their EBM process where the beam is melting the powder by moving back and forth in a snake like way. This in general leads to a microstructure showing a columnar grain where the grains are aligned parallel to the build direction [1][2]. This anisotropy is a result of the occurring solidification conditions in the EBM process and is mainly driven by the solidification rates and thermal gradients within the melt pool. This crystallographic anisotropy leads also to anisotropic mechanical properties which are often not desired. One promising approach to reduce the anisotropy could be using a point melt strategy instead of the traditional cross-snake hatching strategy. Process parameters such as point distance, spot time and beam current are varied to investigate and possibly provoke if an equiaxed or a columnar microstructure in the bulk material is achievable [2].

1.1.2 Aim

The purpose of this study is to find a process window for point melting that results in dense specimens which contain acceptable amounts of defects such as porosity and an uneven melt surface. The effect of the following process parameters on porosity and microstructural features will be investigated: *Beam current [I*], *Point distance [d]* and *Spot time [t]*.

1.1.3 Limitations

Specimen geometry is restricted to cubes with dimensions of 15mm x 15 mm x 25 mm (X, Y, Z). While thickness and width of the specimens are satisfying the geometry specified, the height of some specimens does vary and is not always 25 mm. Characterization of mechanical properties will be limited to a traditional Vickers hardness test. Porous specimens will not be subject for extensive microstructural investigations as compared to dense specimens.

2 Theoretical background

This section is including relevant theoretical aspects and a general background to have a good understanding of the project.

2.1 Additive manufacturing

Additive manufacturing (AM) is a technology where objects are created layer by layer based on a 3D model. This helps to reduce waste of raw material during manufacturing process and most noticeably reduction in tooling time compared to conventional processes [3]. AM also enables more freedom in design as for example possibility to design with internal cooling channels and more complex geometries are made possible.

2.1.1 Electron Beam Melting process

In principle, an EBM machine consist mainly of the following parts: There is a vacuum chamber with an electron-gun on top of it and an electrical cabinet. The schematics of the chamber and the gun on top is shown in Figure 2.1. In the electron gun electrons are emitted from either a tungsten filament or a LaB_6 single crystal when a current passes through [4]. Afterwards the electrons are accelerated to 60 kV to create an electron beam. Focus, astigmatism and deflection coils are used to control and move the beam during processing within the build area with a fast movement of up to 8000 m/s [5]. The kinetic energy of the electrons upon impact causes the melting of the powder.

The EBM process consists of mainly four steps and could be seen in Figure 2.1b. In the first stage of the process, the powder is distributed from the reservoir in the hoppers on to the build plate using a rake system as seen in step 1 in Figure 2.1a. The rakes then move from one side to the other to spread the next layer of powder as indicated in Figure 2.1a by the small red double-edged arrow. In the second stage, the spread powder is pre-heated and lightly sintered at approximately 670° C. This temperature is kept during the whole duration of the build in order to better control residual stresses and minimize the risk of rapid cooling that could lead to unwanted phase transformations. During the third step, the powder is heated up to above the material specific melting temperature where the powder is melted. During the last step of the process the build (start) plate which is mounted on the platform (seen in Figure 2.1a) is moved down a step which is equal to the powder layer thickness and the cycle restarts again until the build is completed.

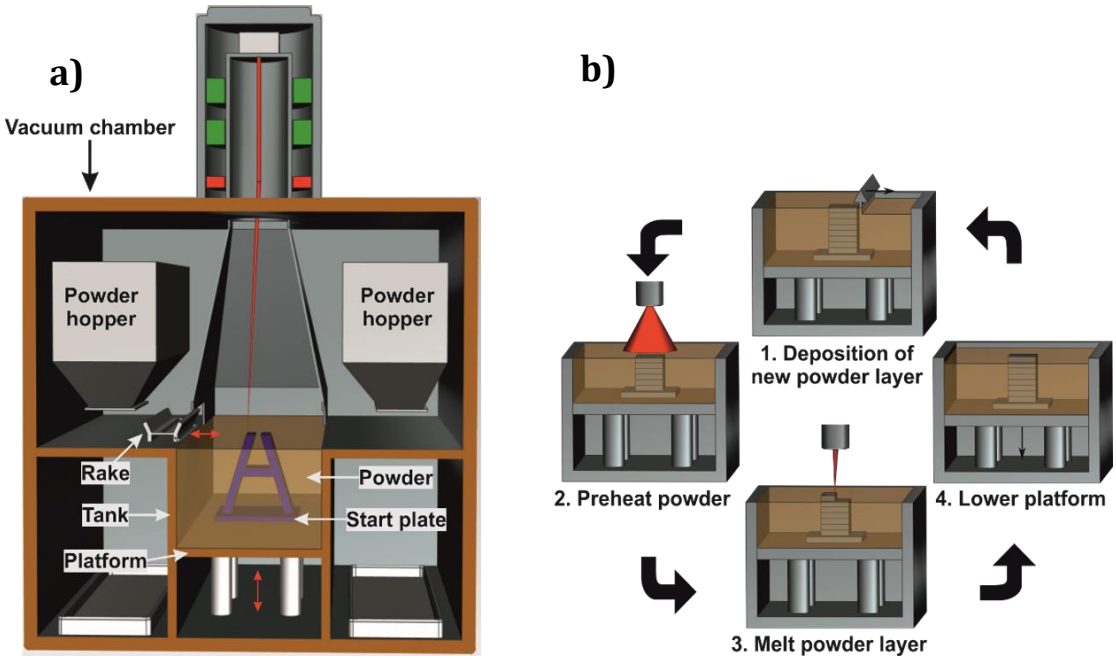

Figure 2.1 ***a)*** *Schematic cross section of the EBM equipment* ***b)*** *Four different steps of the EBM process cycle, permission to use by Markus Ramsperger* [6].

The build process from start to finish is performed in a controlled vacuum atmosphere of approximately 10^{-5} Torr. Additionally, during the melting process partial helium pressure decreases the vacuum to 10^{-2} Torr which enables better cooling ability in the process as well as improved stability during the beam scanning [7].

The powder bed is kept at a material specific build temperature between 300 − 1100°C during the build and slowly cooled to room temperature after the build [8]. First layers of powder form a pre-sintered support structure. This step provides the following built part with mechanical support and routes of heat conduction. Another reason for pre-sintering is to minimize the smoking effect. Smoking can occur when the negatively charged electrons interact with the powder particles in the powder bed [9].
By sintering the powder, the conductivity of the powder increases and at the same time the forces holding the particles together are stronger than electrostatic repulsive forces that repel the particles away from each other and the risk of smoking is thereby reduced [9] [10]. Another way to minimize the risk of smoking is to have helium gas present in the build chamber. Helium prevents the risk of charge build up among the powder particles and thereby decreases the risk of smoking [9]. The helium gas is also there to protect the chemical integrity of the powder material at higher temperatures and to protect against oxidation [11].

2.2 Scanning strategy

In EBM, different scan strategies can be utilized. One frequently used scan strategy is the Hatch scan strategy where the outer outline of the geometry is scanned (contouring). In the next stage usually referred to as hatching the beam is rastered back and forth until one layer of the powder is melted [12]. This process is continued until the desired number of layers are melted.

2.2.1 Process parameters

In the EBM process, several important process parameters can be changed independent of each other to achieve the desired scan strategy objectives. All the parameters explained further can be variable. The layer thickness is traditionally constant throughout a build, but it can theoretically be changed as well. The remaining parameters are variable but are depending on desired scanning strategy.

- Scanning speed [mm/s] is the speed at which the electron beam is moved/scanned across the powder bed.

- Beam current [mA] can be explained by the number of electrons emitted from the electron gun.

- Focus offset [mA] affects the beam spot size. The same effect can be achieved by increasing the beam current. Given constant beam current the spot size increases with increasing focus offset and thereby the energy input decreases.

- Line offset (Hatch spacing) is the distance between two different passes as the electron beam scans the powder bed. Line offset is illustrated in Figure 2.2b.

- Layer thickness [µm] is the thickness of the spread powder layer.

Beam power is defined as given in Equation 1.1. Arcam Q10 machine works at constant 60 kV which leads to that the beam power is directly related to the variations in the current.

$$W = I * V \tag{1.1}$$

The volumetric energy $[\frac{J}{mm^3}]$ measured in Arcam EBM Hatch scan strategy is given in Equation 1.2 [2][13].

$$\text{Energy input}_V = \frac{\text{voltage (kV)} * \text{current (mA)}}{\text{scanning speed } \left(\frac{\text{mm}}{\text{s}}\right) * \text{layer thickness (µm)} * \text{line offset (µm)}} \tag{1.2}$$

2.2.2 Hatch strategy

Hatch scan is traditionally the main technique used by Arcam during melt process of the powder. First, the beam melts the contour of the part geometry as shown in Figure 2.2a. The electron beam moves horizontally from one side of the build plate to the other, i.e. in a bi-directional mode as shown in Figure 2.2b and c. As the horizontal scan given in Figure 2.2b is completed, the beam starts the melting process for the next layer in the vertical mode as shown in Figure 2.2c.

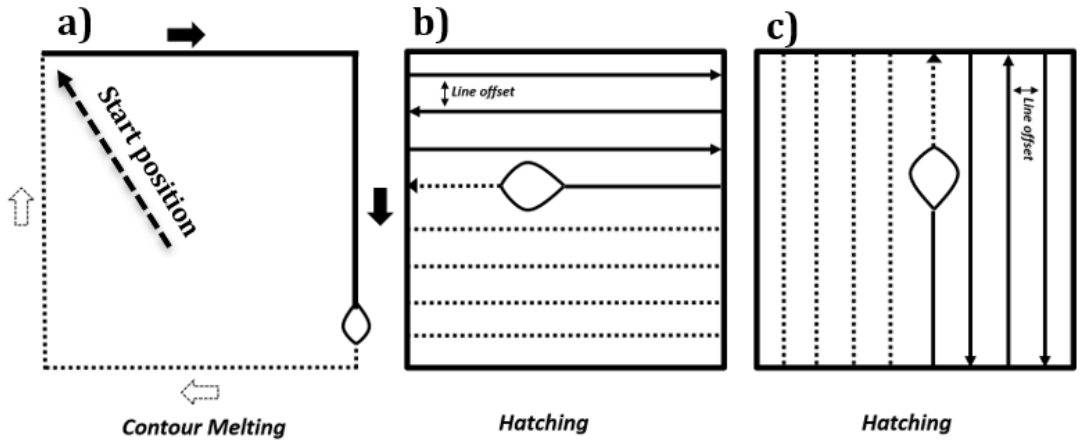

Figure 2.2 Illustration of hatch scan strategy, dashed lines illustrate non-melted powder. Arrows indicate beam movement direction **a)** Contour scan **b)** Horizontal scan **c)** Vertical scan, inspired by Markus Ramsperger [14].

2.3 Titanium and its properties

2.3.1 Background

Titanium is classified as a light and non-ferrous metal. In 1910, titanium was achieved as an isolated metal by heating titanium tetrachloride (TiCl4) with sodium in a steel bomb. In 1932, larger quantities of titanium were processed by combining TiCl4 with calcium. In a later stage of the process development, calcium was replaced by magnesium, and titanium is today mainly produced from the "Kroll process". Titanium is currently ranked as the ninth most common metal and the difficulty of finding it in high concentrations and in pure state makes it expensive. Today, the prime consumer of titanium alloys is the aerospace industry. However, there are also other markets such as architecture, medicine, sports, marine etc [15].

2.3.2 Metallurgy of pure titanium

Pure titanium exists as stable hexagonal close packed (HCP) crystal structure at temperatures below 882±2°C and is referred to as α-titanium. Above the transus limit temperature (882°C), titanium exists as body centered cubic (BCC) crystal structure and is referred to as β-titanium.

The two crystal structures form by an allotropic transformation and this gives titanium large variety of properties. Plastic deformation and rate of diffusion are closely connected to the crystal structure. The HCP structure of α-titanium leads to an anisotropic Young's modulus, i.e. the properties are depending on the direction of the load [15].

2.3.3 Chemical composition and mechanical properties of TiAl6V4

The TiAl6V4 alloy is by far the most used titanium alloy and more than 50% of all titanium alloys used today are of this composition. The two main reasons to the success of this alloy are the good balance of properties and this is why it is also by far the most developed and researched titanium alloy [15].

TiAl6V4 alloy is used in freeform manufacturing of prototypes in racing and in aerospace applications. It is also frequently used in biomedical applications as knee, hip and other joint replacements [16].

The mechanical properties of the alloy can be tailored by alloying and processing [15]. The alloy inherits its properties such as density and elastic modulus by solid solution strengthening and age hardening.

Traditional titanium alloys have very high specific strengths and corrosion resistance [17]. Yield strength of titanium alloys is in a range of 800 to 1200 MPa depending on microstructure [15]. Table 1 and Table 2 shows the chemical composition and mechanical properties of TiAl6V4 alloy produced by EBM compared to cast material and wrought material.

Table 1 TiAl6V4 chemical composition "Titanium alloy Arcam", inspired by [18].

Element	***Arcam Ti6Al4V***	****Ti6Al4V ASTM F1108 Cast material***	*****Ti6Al4V ASTM F1472 Wrought material***
Aluminium, AL	*6%*	*5.5-6.75%*	*5.5-6.75%*
Vanadium, V	*4%*	*3.5-4.5%*	*3.5-4.5%*
Carbon,C	*0.03%*	*<0.1%*	*<0.08%*
Iron, Fe	*0.1%*	*<0.3%*	*<0.3%*
Oxygen, O	*0.15%*	*<0.2%*	*<0.2%*
Nitrogen, N	*0.01%*	*<0.05%*	*<0.05%*
Hydrogen, H	*0.003%*	*<0.015%*	*<0.015%*
Titanium, Ti	*Balance*	*Balance*	*Balance*

**ASTM F1108 (cast material)*
***ASTM F1472 (wrought material)*

Table 2 TiAl6V4 Mechanical properties, inspired by [18]

	Arcam Ti6Al4V	*****Ti6Al4V ASTM F1108 Cast material***	******Ti6Al4V ASTM F1472 Wrought material***
Yiled Strenght (Rp 0.2)	*950 MPa*	*758 MPa*	*860 MPa*
Ultimate Tensile Strength (Rm)	*1020 MPa*	*860 MPa*	*930 MPa*
Elongation	*14%*	*>8%*	*>10%*
Reduction of Area	*40%*	*>14%*	*>25%*
Fatigue Strength* @600 Mpa	*>10,000,000 cycles*		
Vickers Hardness	*330HV*		
Modulus of Elasticity	*120 GPa*		

**After Hot Isostatic pressing (HIP)*
***ASTM F1108 (cast material)*
****ASTM F1472 (wrought material)*

2.3.4 Deformation mechanism

During the α/β transformation and cooling through the β phase field, the most densely packed planes of the BCC phase, {110}, transform to {0001} planes of HCP phase. Since the distance between the basal planes in HCP phase is larger than the corresponding distance in BCC phase, there will be a minor atomic distortion in the c/a ratio of the HCP structure due to a contraction of the c-axial distance [15].

HCP α-titanium has a more restricted plastic deformation capability compared to BCC β-titanium. This behavior is explained by the amount of slip systems available in different crystal structures which is 3 for HCP and 12 for BCC.

Transformation of the slip planes of the BCC β-titanium to the basal planes of HCP α-titanium is represented in the Burgers relationship (Equation 1.3):

$$\{0001\}\ \alpha\ //\ \{110\}\ \beta \text{ and } \langle 1120\rangle\ \alpha\ //\ \langle 111\rangle\beta \qquad 1.3$$

In the β-titanium unit cell, the corresponding six slip planes and two slip directions give a total of 12 different α-titanium growth orientations inside the prior β-grains [15].

2.3.5 Oxidation of TiAl6V4

The chemical affinity of titanium to oxygen is high and increases with increasing temperature which explains the need for inert build atmosphere in the EBM process [19] [11]. Due to the high chemical affinity the outer surface forms a passive oxide layer of TiO2 even at room temperature [20]. At higher temperatures, i.e. at around 500°C, TiAl6V4 alloys oxidize rapidly and form a brittle oxygen enriched layer which is detrimental to fatigue life in specially dynamic loading [21].

2.4 Titanium alloys classification

2.4.1 Stabilizing elements

Based on the chemical composition, titanium can be classified into α, α + β and β alloys [19] [22]. Alloying elements help increase or decrease the α/β transus temperature as shown in Figure 2.3. Al is a substitutional α-stabilizer while O, N and C acts as interstitial α-stabilizers. Mo, V, Ta, Nb, Fe, Mn, Cr, Co, Ni, Cu and H acts as β-stabilizers. The α-stabilizing elements O, N and C increase the strength of the alloy at the cost of ductility [19]. Figure 2.3 illustrates the effect of α and β-stabilizers on the β-transus temperature as the concentrations varies.

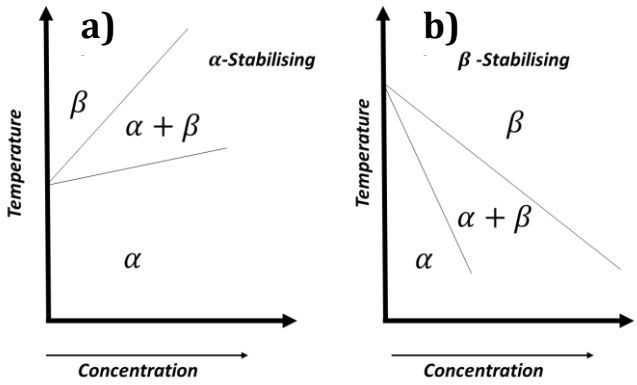

Figure 2.3 Effect of stabilizers on the β-transus temperature ***a)*** *α-stabilizers* ***b)*** *β-stabilizers, inspired by* [21].

2.4.2 Alpha, α Alloys

Alpha phase has HCP crystal structure at room temperature and shows good creep performance, low ductility and high density. Aluminum is the main alloying element. The material shows the highest strength and resistance to oxidation at elevated temperature although the strength at room temperature is low. Alpha alloys

are not applicable to strengthening by heat treatment because they are single phase alloys [19].

Alpha phase is apparent in form of primary or secondary α, also known as transformed β. Primary α can be observed after prior hot work. Secondary α is observed after transformation from β which appears after cooling above β-transus. Secondary α can also be formed by aging from high temperatures within α + β field [23]. Annealing of cold-worked alloys above the recrystallization temperature results in equiaxed α while elongated α grains can be obtained by directional work of the alloy [23].

2.4.3 Beta, β Alloys

The main characteristics of β alloys are the excellent hardenability properties due to the heat treatable nature of the alloys. β possesses limited high temperature strength while room temperature strength is good [24]. These alloys contain enough β-stabilizing elements (see section 2.4.1) which help to suppress the martensite start temperature below room temperature when quenched [19].

Equilibrium β is present in smaller amounts in α + β alloys at room temperature. At room temperature, β phase can also be present as a metastable phase in alloys containing enough β-stabilizing elements while cooled rapidly [23].

2.4.4 Alpha + Beta (TiAl6V4)

TiAl6V4 consists of α and β phases due to presence of 4-6% β-stabilizing elements such as Vanadium. Acicular (Plate-like) alfa prime (α′) exist in α + β titanium alloys as HCP-phase upon rapid cooling from β-phase field [22]. Multiple forms of acicular martensitic/non-martensitic phases can be formed upon rapid cooling. These variations of available phases depending on process parameters requires rigorous characterization to differentiate between the different phases [22]. Vanadium helps the material to achieve good room temperature ductility while aluminum acts as α phase stabilizing element and helps to increase the strength of the alloy [25]. The β phase helps to improve the materials ability to undergo a heat treatment process [24]. The single-phase solidification of α + β TiAl6V4 helps to limit the appearance of solidification related cracking which results in good strength, ductility, formability and fatigue properties [25] [19]. This category of titanium alloy shows restricted creep performance which results in maximum operation temperature of $300 - 350°C$.

2.5 Microstructure of TiAl6V4

2.5.1 Microstructure of EBM-produced TiAl6V4

EBM fabricated TiAl6V4 has a fine microstructure when compared to wrought and cast materials due to fast cooling rates of up to 1000°C/s [19]. The material is liquified at around 1900°C in the two phase region and rapidly cooled down to 700°C [1]. For TiAl6V4 the build is maintained at 670°C and slowly cooled to room temperature after the build is completed. Columnar grains are growing epitaxially and parallel to the build direction. α-laths grow at the prior β-grain boundaries. The β-grain boundaries contain a microstructure of Widmanstätten α-platelets and rod-shaped β [1] [19].

The geometry of the built specimens and the process parameters affect the shape of the grains formed as the different parameters contribute to different thermal behavior during cooling of melt pools. The high beam velocity, small spot sizes as well as the low conductivity of titanium tends to result in elongated melt pools. These melt pools have a length/width aspect ratio of 5:1 and an even larger length/depth ratio of 20:1 [26]. It can also be observed that height and diameter of the previous β grains are dependent on such process parameters. As the scan speed, beam current and focus offset increases, so will the size of the prior β grains which can be related to increased energy density in the EBM process of TiAl6V4 melting [1].

2.6 Solidification and diffusion

Densely packed atomic planes of HCP α-titanium result in a much lower diffusion coefficient than the less densely packed atomic planes of BCC β-titanium [15]. The microstructure of the alloy also affects the diffusion coefficient of the respective phases and has implications on the mechanical behavior of the two different phases.

The mode of solidification affects properties such as size and shape of formed grains but also presence of inclusions, defects such as porosity and cracks [19]. The growth mode after nucleation is dependent on thermal gradient (G) and growth rate (R) in the solid/liquid interface. Planar, cellular and dendritic solidification is possible depending on the previously mentioned parameters.

Heterogeneous solidification of TiAl6V4 occurs like in a pure metal due to the very narrow solidification range of 550°C. This fact together with lack of segregating elements and phases that melt at low temperature result in low susceptibility to solidification related cracking [19].

Phase transformation of $\beta => \alpha'$ depends on the cooling rate. At temperatures close to Tm (melting temperature) and slow cooling rate, the diffusion process dominates and growth of fewer nuclei are more thermodynamically favorable. At larger undercooling and faster cooling rate the barrier to nucleation is much lower and more nuclei are nucleating as the diffusion process is slower, see Figure 2.4 [27]. The total transformation rate is the a product of the diffusional process (growth rate) and formation of nuclei (nucleation rate)[28]. A finer grain structure is obtained in the material at higher cooling rates. Diffusional transformation of $\alpha' => \alpha + \beta$ occurs once the material is aged at around 750°C.

The α lamellae which have formed during cooling from the β phase have a lower concentration of elements such as oxygen which helps the age hardening as Ti_3Al intermetallic phase is formed as a precipitate. The age hardening occurs at temperatures below 600°C. Ti3Al precipitates at 550°C that leads to that any aging above 550°C leads only to stress relieve and no hardening effect [29].

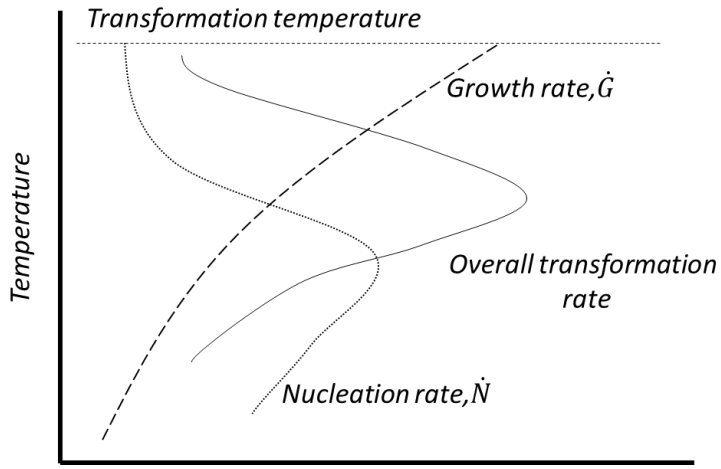

Figure 2.4 Graph illustrating the relationship of nucleation rate, growth rate and overall transformation rate, inspired by [28].

2.7 Cooling rate effect on microstructure

The melt pool is cooled down from 550°C to the build temperature (670°C) with a high cooling rate where the diffusionless martensitic transformation occurs and the $\beta \rightarrow \alpha'$ transformation is completed. In the next part of the process the component is kept at build temperature and α' decomposes into $\alpha + \beta$ [16].
For complete decomposition of α' to $\alpha + \beta$ to occur the build should be kept at 700°C for around 30 minutes [1]. In the final stages of the process the temperature decreases from build temperature to room temperature at a slow rate without any further phase transformation.

At the cooling rate of >410°C complete martensitic transformation is possible. Martensitic phase formation gradually decreases down to cooling rates of 20°C 20°C/s at which it will not be possible to form more martensitic phase. As the cooling rate is decreased, the microstructure formed will be more and more Widmanstätten α-titanium [19]. The size of the newly formed α is restricted by the previous β grain. α also grow until they meet another α grain. On the contrary, the size of the β rods are similar in all specimens even with change of process parameters and specimen size. This can be explained with the similar nature by which the β and $\alpha + \beta$ phase is [16] formed as all specimens are cooled down and kept at 670°C for the same amount of time [1]. As the energy input increases, the size of α' and $\alpha + \beta$ lamellae increase. The repeated heating cycles during the EBM process induce heat on the previous layers which leads to coarsening effects of the grains. Holding temperatures between 700 and 800 °C have a coarsening effect on the α-lath size while a holding temperature of approximately 600°C result in a small coarsening effect of the α-lath size independent of holding time [16].

2.8 Types of porosity seen along the build direction

Two types of porosities are characterized. Pores created by entrapped gas in the powder material have a spherical morphology. The other type of pores seen in EBM melted titanium are irregularly shaped non-sintered areas parallel to each build layer, called lack-of-fusion. Traces of non-melted powder can be found inside

these irregularly shaped defects which confirms that they originate from non-sintered areas [8] [30].

Mechanical properties are affected by the amount of porosity present in the specimen. In applications where, cyclic loading is applied the porosities can act as crack nucleation sites and result in premature failure. Lack of fusion porosity is most detrimental to the mechanical proprieties in loading scenarios where the load is applied normal to the build direction. This is explained by planar shape of non-melted areas normal to the build direction [30]. Figure 2.5 illustrates the other types of porosities, including gas porosity and lack of fusion. The build direction is illustrated by the white arrow.

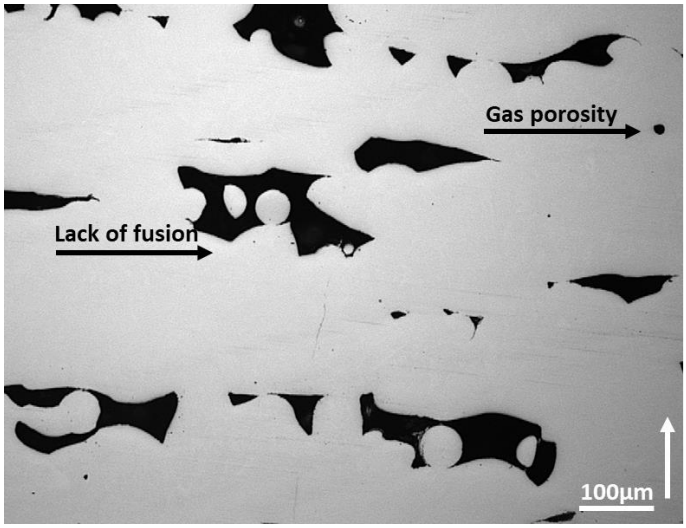

Figure 2.5 Typical lack of fusion and gas porosity defect as observed with respect to the build direction (BD).

3 Methods

The following methods are used to remove defective specimens in a step by step process based on the quality of each specimen's distance, spot time and volume energy on specimen quality is obtained based on information and data gained from the methods used.

The amount of acceptable porosity without detrimental effect to mechanical properties of the material is set to 0.2% area fractions (Af%) in agreement with Arcam. Specimens with densities below 99.8% are regarded as defective.

The difference in time at which the first layer and last layer are exposed to higher temperature (670°C) can be up to 4 hours during each build. This means that as the first layer is exposed to the process build temperature of 670°C, there is going to be an increasing aging process further away from the last melted layer.

3.1 Point melt strategy in this project

The point melt strategy in this project is illustrated in Figure 3.1. Point 1 is melted first followed by point 2. They are separated by a horizontal distance equal to x. This distance is referred to as point distance. Later, the beam moves one distance equal to y upwards to the following row and point 3 and 4 are melted. As this process is continued until point 10 is melted, the process continues with the next column marked with dashed contour. Once the layer is melted the whole grid is rotated 90 degrees and the process is repeated again [2]. In addition to the parameters introduced in section 2.2.1, three additional parameters will be introduced for the point melting strategy.

- Spot time [ms] is the duration of which the beam is focused on a single spot (point).
- Number of points in each layer.
- Point distance [mm] the distance between two points as seen in Figure 3.1 illustrated by x and y.

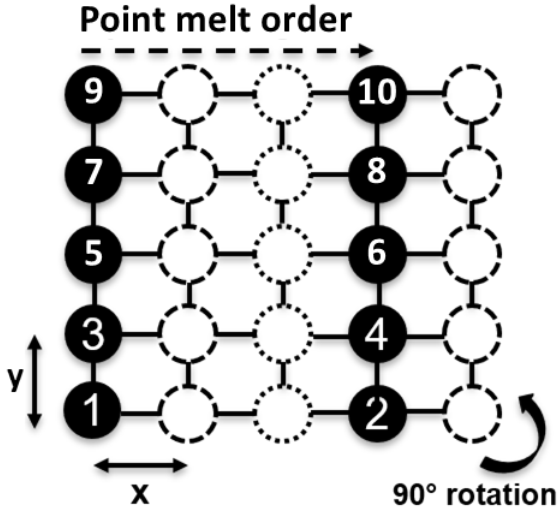

Figure 3.1 Illustration of point melt strategy.

The volumetric energy density for the point melt strategy is given by Equation 1.4 [2].

$$\text{Energy density}_v = \frac{\text{current (mA)} * \text{spot time (ms)} * \text{voltage(kV)}}{\text{layer thickness (µm)}} \quad (1.4)$$

The traditional hatch scan strategy can be characterized with a line and volume energy whereas the point melting strategy in this work is characterized by the volume energy $\text{VE} = \frac{\text{J}}{\text{mm}^3}$ as basis of most analytical investigations. This is because line energy would not be enough to investigate the energy input as a line cannot be defined continuously between more than two specific points. This can be seen in Figure 3.1 where the beam scans point "1" and "2" and continues with point "3" and "4" which are shifted one row in the y-direction. This means that the two points (illustrated in the figure by dashed circles) between point "1" and "2" are not treated at the same time and thereby a line energy quantification would not be feasible.

Volume energy (VE) [J/mm^3] is one important parameter in this work and depends on beam current [mA], spot time (ST) [ms], point distance (PD) [mm], and number of spots.

Spot time is the time which the beam is focused on a single point. Point distance is the distance between two separate points on the powder bed. Spot time and point distance are the same for all specimens belonging to the same build plate. Beam current is variable between specimens in the build plate and is increasing from first specimen in the build plate to the last. Number of points vary with each different build plate which means that specimens from the same build plate have the same amount of points. There is an inverse relationship between spot time and number of points. As the number of points decrease the point distance and spot time increase to maintain same volume energy input between specimens in the different build plates. This is of importance to the project to compare microstructural evolutions and mechanical properties based on volumetric energy.

3.1.1 Specimen orientation and naming scheme

Five different build plates with up to 16 specimen/plate were produced in an Arcam Q10 machine. Each specimen is produced with varying process parameters (insert range variation). Parameters can vary between each build plate but also within each build plate. The build plate (start plate) is made from stainless steel. During the build process the chamber is kept at approximately 670°C regardless of build plate. The temperature is measured just below the build plate which means that a specific specimen temperature is not obtained but rather a general temperature in the areas close to the build plate is measured. The position of each specimen on the build plate is specified in Figure 3.2 with corresponding build order.

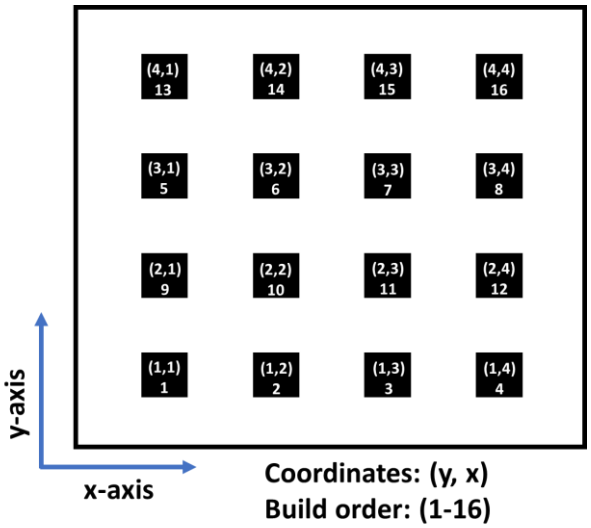

Figure 3.2 Build plate building sequence.

Each specimen is named with its respective build plate (BV) and build order number as illustrated by Figure 3.2. Specimen 1 from the first build plate is named as BV1.1 and specimen 2 is thereby called BV1.2. Further data regarding each separate specimen is provided in Appendix 1: Specimen naming. The build sequence is chosen to achieve less difference in thermal gradients. This means that as specimens (cubes) 1-4 are fabricated the following specimens 5-8 are offset an entire row as can be seen in Figure 3.2.

3.1.2 Process parameter range

The range variation of chosen process parameters in this project can be seen in Table 3. Build plate 1-5 are given on the left side of the table. Point distance, number of points and spot time are parameters which are fixed for each build plate and can be seen in the table. Current, energy of all points and volume energy are given with a range from the smallest value to the largest. Further information for each specimen is given in Appendix 1: Specimen naming.

Table 3 Range of process parameter variation.

	Point distance [mm]	**Number of points [#]**	**Current [mA]**	**Spot time [ms]**	**Energy all points [J]**	**Volume energy [J/ mm^3]**
BV1	0.2	5626	1.67-9.17	0.4	225-1237.5	20-110
BV2	0.1	22500	1.17-8.67	0.1	157.5-1170	14-104
BV3	0.5	900	2.67-10.17	2.5	360-1372.5	32-122
BV4	0.3	2500	2.17-9.67	0.9	292.2-1305	26-116
BV5	0.5	900	10.67-30	0.25	540-1777.5	48-158

3.1.3 Powder characteristics

Powder used in this project is the standard Arcam TiAl6V4 plasma-atomized powder with a size distribution 45 − 106 µm. The powder layer thickness is 50 µm according to standard Arcam settings before sintering [11].

3.1.4 Limitations for point melt applications in Arcam Q10

A limiting factor for developing a point melt strategy in EBM is the internal sampling rate of 250 kHz of the EBM system. That means for the development on the one hand side that the minimum applicable point time is limited to 40 µs. On the other side, the minimum jump time between the points is limited to approx. 30 µs since focusing and jumping is much faster than the sampling rate for melting. This must be considered when choosing the point distance and the number of points, respectively. Especially when the melting times and energies should be held constant within the experiments. As a result, jump time increases if the number of spots and distances between spots increases.

3.2 Specimen preparation

3.2.1 Sectioning

Silicon carbide sectioning wheels are used to cut the cubes with Struers Disctom-2 cutting machine. The specific cutting disc is according to Struers standard 20S30 for soft non-ferrous materials. Sectioning was performed in two different cross sections according to Figure 3.3a and b. To avoid risk of un-sintered powder causing scratches in the following polishing steps, a first sectioning was performed along the xy-plane according to Figure 3.3a. The sectioning was performed just above the support structure (black-dotted section of the cube) to separate the specimen from the support structure. Further on the specimens were sectioned along the yz-plane according to Figure 3.3b.

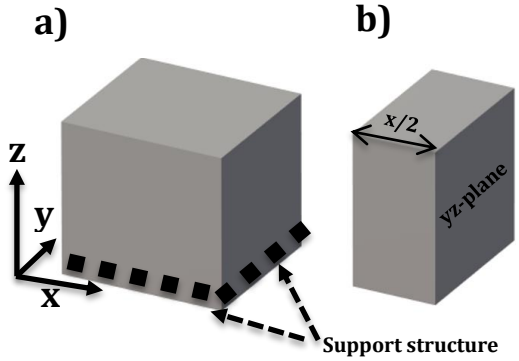

Figure 3.3 Specimen shown in two different stages of the sectioning process **a)** As received state with removal of support structure **b)** Sectioning performed along the yz-plane along the build direction.

3.2.2 Mounting

Struers Polyfast hot-mounting powder is used to mount the specimens in 40mm and 30mm wide cylinders. The mounting is performed by Struers CitoPress-20 at 180°C for a duration of 5 or 6 minutes depending on specimen diameter where the larger specimens were mounted for 6 minutes and the smaller for 5 minutes.

3.2.3 Grinding and polishing

Struers TegraPol31/TegraForce-5 was used during polishing and grinding. A five-step grinding is performed according to Struers standard with smaller modification to suit this specific material. Silicon carbide sandpaper of grit size 200, 500, 800, 1200 and 2500 is used for the grinding process. If required, an optional grinding with grit 4000 was performed. Experimental trials with the above-mentioned grinding papers resulted in a good quality surface for polishing in the subsequent step. A Struers MD-Chem cloth was used together with a mixture of 50bml colloidal silica (OP-S), 50 ml distilled water and 10 g potassium hydroxide chemical solution for the chemical-mechanical polishing. The polishing with MD- Chem cloth was performed for a duration of 180-300 seconds depending on specimen. All specimens were carefully cleaned under running water during the first two to three steps of the grinding to remove retained pieces of the material on the surface of the specimen. Cleaning in an ultra-sonic bath was performed for 10 minutes for each specimen before the chemo-mechanical polishing.

3.2.4 Etching

Kroll's etchant (1 ml HF, 2 ml HNO_3 and 97 ml H_20) was used to etch specimens to highlight microstructural features in the light optical microscope. Each specimen was treated gently for about 30-60 seconds. The etching time varied slightly from specimen to specimen. White areas of the etched specimens belong to the primary alpha phase, while β phase appears dark when etched with Kroll´s.

3.3 Imaging of specimen

In this chapter, the different techniques used to capture images for different stages of analysis are explained. A vertical arrow indicating the build direction is seen in the images captured by optical microscope and digital camera throughout the work.

3.3.1 Digital camera

Images of each specimen were taken with a digital camera for further characterization of the porosity and swelling. Surface and side walls of specimens with no clear sign of defects such as swelling or rough side walls are shown in Figure 3.4a and b. These images will be the basis for the first specimen classification which will be further discussed in section 4.1. The point structure is visible as can be seen in Figure 3.4a where the different points represent one pulse of the electron beam. Figure 3.4b shows the support structure at the bottom of the printed specimen.

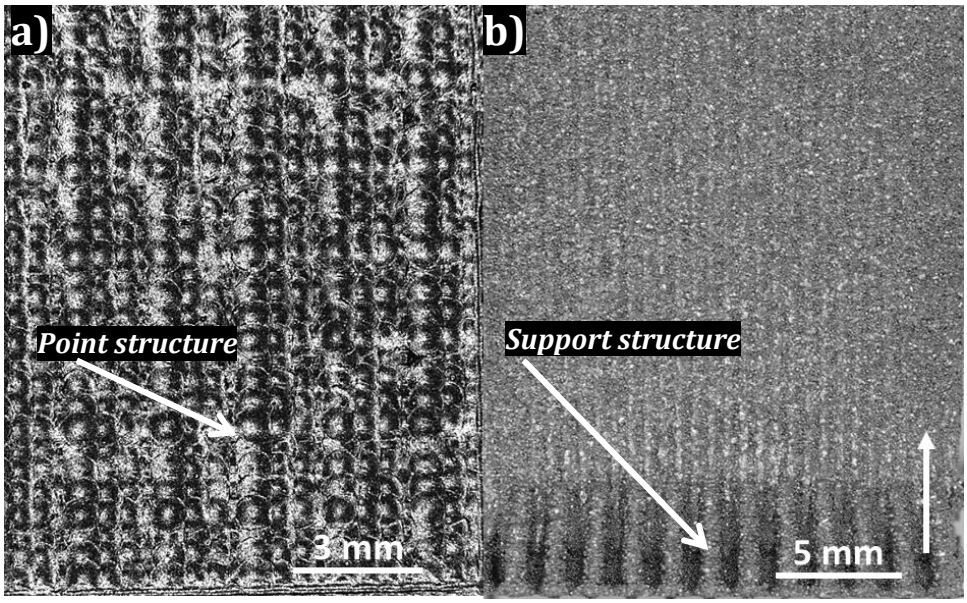

Figure 3.4 ***a)*** *Surface of specimen with visible point structure (circles)* ***b)*** *Side walls and bottom part including support structure.*

3.3.2 Investigations by Optical microscopy

A Zeiss Discovery.V20 stereo microscope was used to acquire images of specimen surfaces. Images illustrating the overall topography of each specimen are captured to further characterize the defects such as porosity and swelling. Moreover, images are taken of specimens that are fulfilling the requirements for further analysis. Images were captured at 100 times magnification using a LOM Leitz DMRX microscope. In polished state, images were captured 2mm below the specimen surface from one side to the other for porosity measurements. Images were also acquired at different magnifications in etched state for microstructural analysis.

3.4 Image analysis using ImageJ

ImageJ software was used to estimate area fractions (Af, %) of porosity. Images received from the light optical microscope were used as basis for porosity analysis. Images captured from side to side of each specimen were stitched together. A certain threshold is applied, and the software differentiates between areas falling below and above the set threshold value and a binary image is generated. Those areas falling below the threshold were seen as white areas (dense) and those falling above the threshold value are coloured as black areas (pores). As can be seen in Figure 3.5 the binary image (Figure 3.5b) provides a clear distinction between dense (white) and porous areas (black).

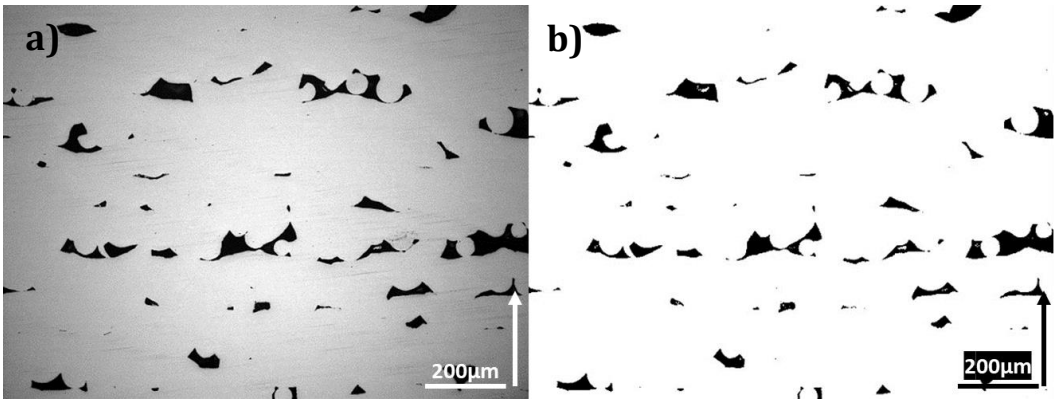

Figure 3.5 Optical micrograph and binary image of specimen surface at 100X magnification ***a)*** *Obtained image from optical microscope* ***b)*** *Binary image obtained after ImageJ software .*

Based on the image in Figure 3.5b, the ImageJ software calculates the area fraction of black area as compared to the total area. As the specimen gets denser, the ImageJ software is not always able to differentiate between pores and dense areas. This is mainly due to the size of the pores are generally smaller in denser specimens and the smaller pores are more difficult to observe at 100X magnification. Images below illustrate the difference in what is accounted as pores with different threshold values. Figure 3.6 shows images of two different applied threshold values, 30 and 60, in the ImageJ software. As seen in the images, it is very difficult to notice any difference in what is accounted for as pores despite the large difference in applied threshold value. Figure 3.6a has a total of 1.063% Area fraction porosity and Figure 3.6b has 1.146 % porosity. This indicates clearly that porosity values obtained based on the images captured by optical microscopy are reliable as no significant variation is observed with different threshold values.

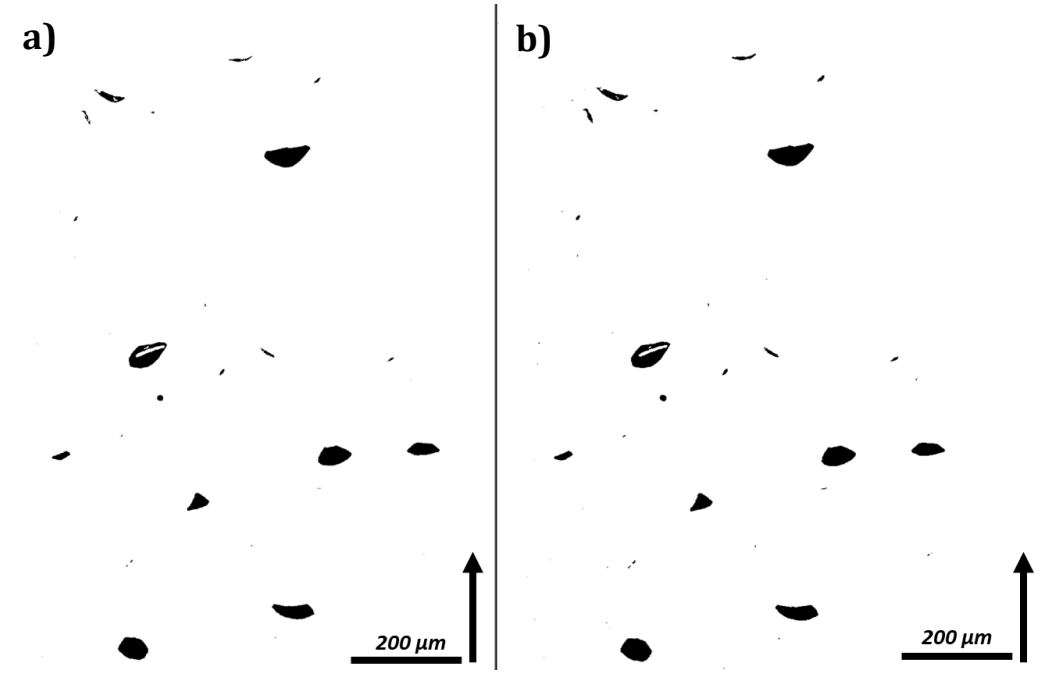

Figure 3.6 Measured porosity at different applied threshold values ***a)*** *Treshold value 30* ***b)*** *Treshold value 60.*

3.5 Hardness testing

Hardness indentation is done according to the Vickers standard ASTM F620. Testing was performed by Strues DuraScan automatic hardness machine at settings of HV1.0 which translates to 1 kg of applied load. A grid is placed manually on the specimen surface in order for the machine to have a determined indentation path as seen in Figure 3.7 with a pattern consisting of rows of three indentations per row. The indentations are 2mm apart from each other in x and y directions. Three indents are made at each row and depending on specimen height 7 to 9 rows of indents are made as shown in Figure 3.7. Rows are numbered from bottom to the top of the specimen. Increasing row number indicates indentations being closer to the surface of the specimen. The hardness measured for each row is the average value of the three indents.

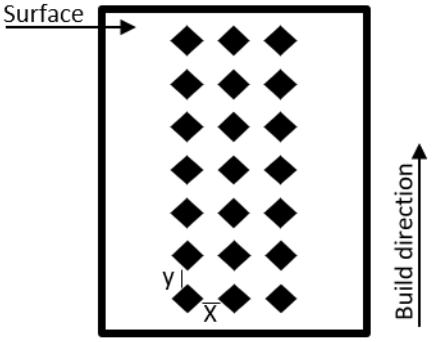

Figure 3.7 Sketch of the indentation matrix made for the hardness measurement.

4 Results

4.1 Specimen classification

The 72 specimens originating from the five different build plates were sorted into three different groups. The specimens were grouped based on images captured by digital camera (side wails) and stereo microscope (specimen surface). The different categories as seen in Table 4 are:

- Porous
- Dense
- Showing swelling and/or showing uneven side walls

Specimens falling into category B "Dense" were investigated further.

Table 4: Different categories of specimen integrity

Porous	Dense	Swelling and/or uneven side walls
A	B	C

Figure 4.1a-d illustrates typical specimen surfaces representing porous (Figure 4.1a), dense (Figure 4.1b), swelling (Figure 4.1d) and uneven side (Figure 4.2a) together with their respective point distance and volume energy. It can be noted that as the volume energy increases the porosity decreases. Swelling becomes an issue at even higher volume energy as seen in Figure 4.1d. Figure 4.1c shows a dense specimen surface at higher magnification.

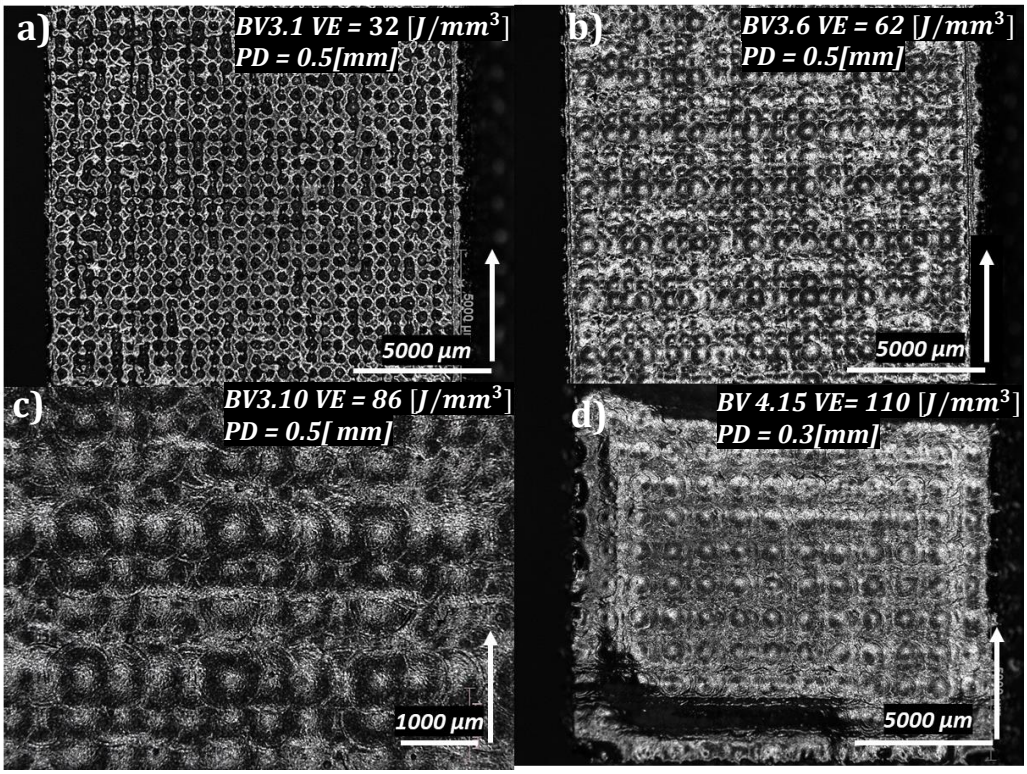

*Figure 4.1 Optical micrographs of the top surface of specimens with different parameters **a)** Porous **b)** Dense **c)** Dense specimen at higher magnification **d)** Swelling.*

Figure 4.2a and b illustrate specimens where the outer surface shows uneven and even side walls, respectively. Specimens BV 5.14 is regarded as defective on basis of rough side walls as the side walls show unacceptable geometrical tolerances. Specimen BV2.8 is considered as acceptable for further investigations as long as no other defects are observed on the top surface.

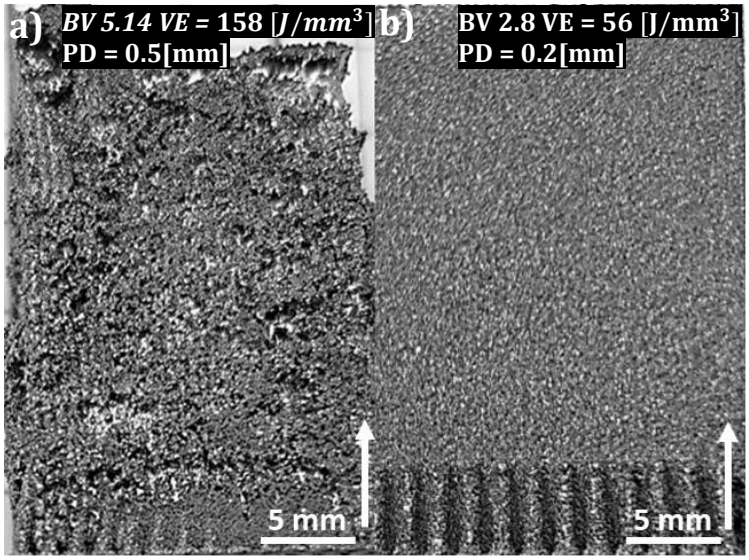

Figure 4.2 Optical micrographs of sidewalls of specimens with different volume energy input ***a)*** *Uneven side walls* ***b)*** Acceptable side wall.

4.1.1 Specimen categorization

Following the classification based on Table 4, all 72 specimens were designated to the different categories (Table 4). This resulted in 42 specimens being disregarded and another 34 specimens falling into category B as basis for further investigations. Table 5 provides the remaining specimens for further investigations. It is also important to note that only one specimen from build plate BV5 is in category B.

Table 5: Specimen quality categorization.

Specimen name	***1***	***2***	***3***	***4***	***5***	***6***	***7***	***8***	***9***	***10***	***11***	***12***	***13***	***14***	***15***
BV1* ***PD = 0.2mm***	A	A	A	A	B	B	B	B	B	B	B	B	B	C	C
BV2* ***PD = 0.1mm***	A	A	A	A	B	B	B	B	B	B	B	B	B	C	C
BV3* ***PD = 0.5mm***	A	A	A	A	B	B	B	B	B	B	B	B	C	C	C
BV4* ***PD = 0.3mm***	A	A	A	A	B	B	B	B	B	B	B	C	C	C	C
BV5* ***PD = 0.5mm***	N	N	N	N	N	N	N	N	C	C	C	C	C	C	B

N = Was not performed.
PD = Point distance
** Specimen naming explained in section 3.1.1.*
** Parameters for each BV series are explained in Appendix* 1: Specimen naming.

4.2 Primary process window

Figure 4.3 provides a primary process window based on the three different categories of specimen integrity as seen in Table 4. Volume energy is given on the y-axis and point distance is given on the x-axis. The four different build plates BV1-BV4 with 8-16 specimens each are shown in the graph. Specimens belonging to BV5 are not illustrated in Figure 4.3 due to only one data point belonging to category B. From this stage specimens belonging to build plate BV5 are not shown in the process window.

The location in the process window for specimens belonging to category B (dense) indicates an existing trend of required volume energy and point distance to yield dense specimens. It is also clearly seen that at the lower end (low volume energy) of the process window porous specimens are observed and at higher volume energies swelling starts to occur. Three images of the specimen surfaces are included in the figure with arrows indicating their respective volume energy. The evolution of varying specimen surface quality from low to high volume energy is illustrated.

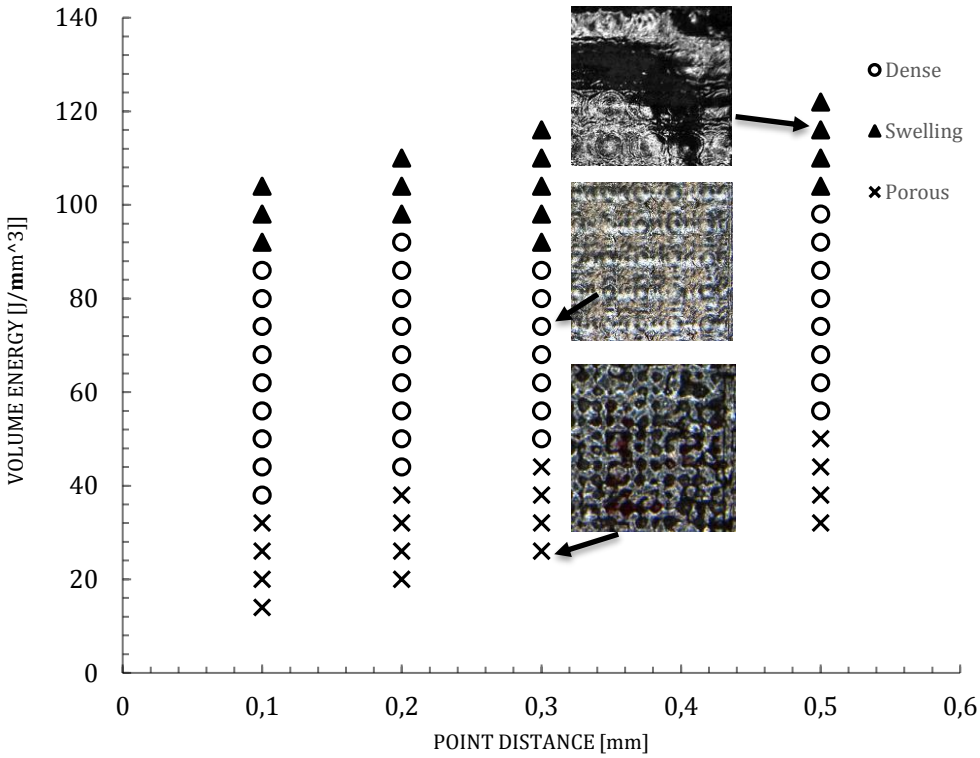

Figure 4.3 Primary process window illustrating first screening of specimen quality. Specimen information in Appendix 1: Specimen naming.

4.3 Porosity

4.3.1 Total porosity measurement

The 34 dense specimens remaining after the first step of elimination (Table 5) are further investigated by Image J software for quantification of porosity based on images captured by use of optical microscopy as explained in section 3.3.2. Total amount of porosity is measured including lack of fusion and gas porosity shown in Figure 4.4. As mentioned earlier, specimens with > 99.8% density are considered dense. Build direction is according to the white vertical arrow.

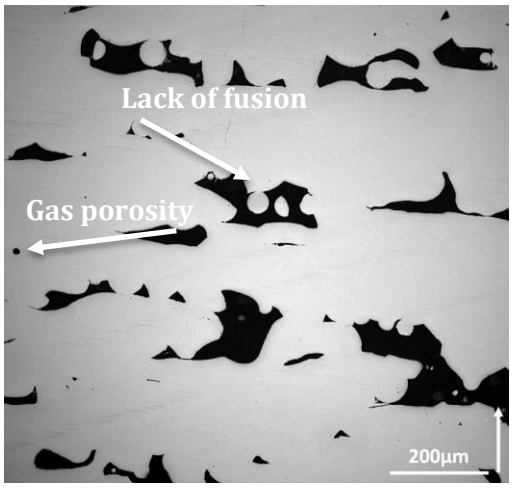

Figure 4.4 Optical micrograph showing lack of fusion and gas porosity in specimen BV2.5.

Figure 4.5a and b show an example of a dense and porous specimen. Different types of porosities are observed with varying size and shape. Figure 4.5a shows a specimen with point distance of 0.3 mm at 62 J/mm^3.Figure 4.5b, showing significantly more porosity, is a specimen with point distance of 0.1 mm at 68 J/mm^3.

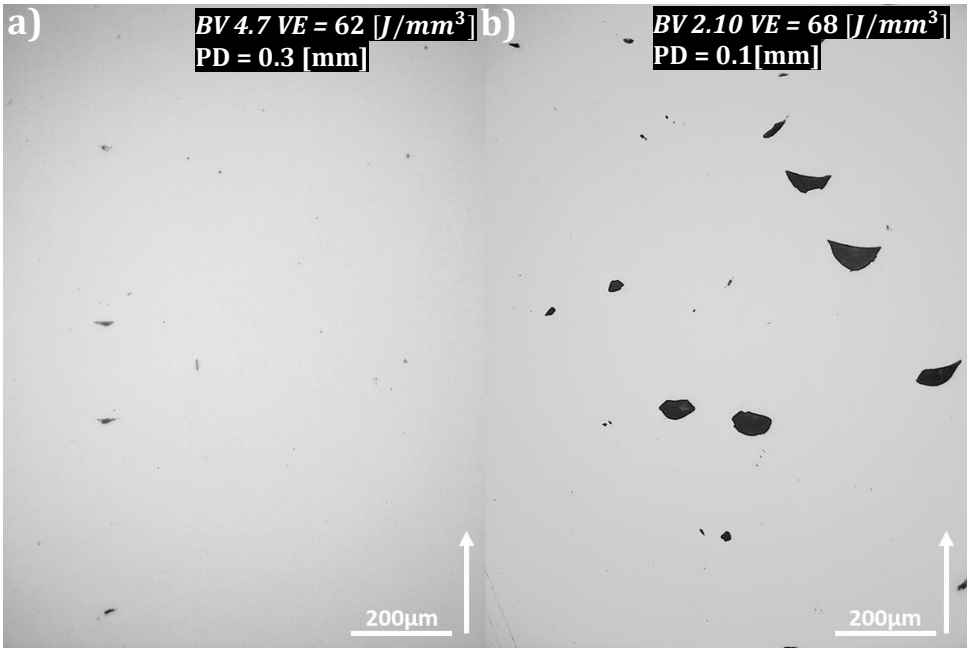

Figure 4.5 Micrograph showing specimen surface and porosity in two different specimens with varying parameters, 100 X magnification ***a)*** *Dense specimen* ***b)*** *Porous specimen.*

A further 15 specimens were disregarded in this elimination process resulting in 19 specimens remaining with a density of at least 99.8%. Table 6 gives total amount of porosity including lack of fusion and gas porosity. Af% values marked with bold numbers indicate specimens falling into the dense category according to the 0.2% Af definition set in this work. Data points showing higher standard deviation value than the mean average can be explained by positional dependency

of the porosity measured. As the porosity is measured from one side of the specimen to the other there is a very big spread in existing porosity between images captured on the specimen surface.

Table 6, Primary porosity measurement.

BV1	**5**	**6**	**7**	**8**	**9**	**10**	**11**	**12**	**13**
Af%	**0,176**	**0,153**	**0,122**	**0,083**	**0,085**	0,491	0,441	0,343	1,433
SD	0,132	0,157	0,094	0,112	0,188	0,46	0,308	0,472	1,049
BV2	**5**	**6**	**7**	**8**	**9**	**10**	**11**	**12**	**13**
Af%	7,05	1,553	0,534	**0,169**	0,208	0,927	0,635	0,88	1,6
SD	1,665	0,707	0,274	0,113	0,095	0,201	0,255	0,254	0,682
BV3	**5**	**6**	**7**	**8**	**9**	**10**	**11**	**12**	**13**
Af%	**0,03**	**0,045**	**0,048**	**0,028**	**0,008**	**0,07**	**0,137**	**0,036**	-
SD	0,023	0,035	0,045	0,024	0,006	0,042	0,145	0,034	-
BV4	**5**	**6**	**7**	**8**	**9**	**10**	**11**	**12**	**13**
Af%	**0,16**	**0,09**	**0,053**	**0,067**	**0,055**	0,229	0,751	-	-
SD	0,084	0,072	0,026	0,095	0,087	0,349	0,688	-	-
BV5	**6**	**8**	**9**	**10**	**11**	**12**	**13**	**14**	**15**
Af%	-	-	-	-	-	-	-	-	0,337
SD	-	-	-	-	-	-	-	-	0,154

**Black arrow indicates higher Volume energy direction*
**SD stands for standard deviation calculated by ImageJ software.*
**Af%, Area fraction of porosity calculated by ImageJ software.*

4.3.2 Measured porosity relation to volume energy input

The relation between point distance and volume energy are provided in Figure 4.6 with density shown on the y-axis in Af%. The different point distances are marked with different symbols on the graphs and their respective volume energy are given on the x-axis. The black horizontal line indicates 99.8% density. It can be noted that at lower volume energies, the specimens indicate a lot of porosity. As the volume energy increases, there is a process parameter window where specimens show dense structure. The span of the window where specimens are dense varies depending on point distance. Given constant volume energy, the specimens with smaller point distance show more porosity. It can also be noted that specimens with smaller point distance also have shorter spot time as compared to specimens with larger point distance.

It is also interesting to observe the sudden increase of porosity after a certain value of volume energy. The graphs show a window after which the occurrence of porosity starts to again. The re-occurrence of porosity is observed at higher volume energy in the specimens with larger point distance compared to lower volume energy in specimens with smaller point distance. As can be seen on Figure 4.6, there is a trend for the specimens with point distance of 0.1 to 0.5 that indicates less porosity in the specimens with larger point distance.

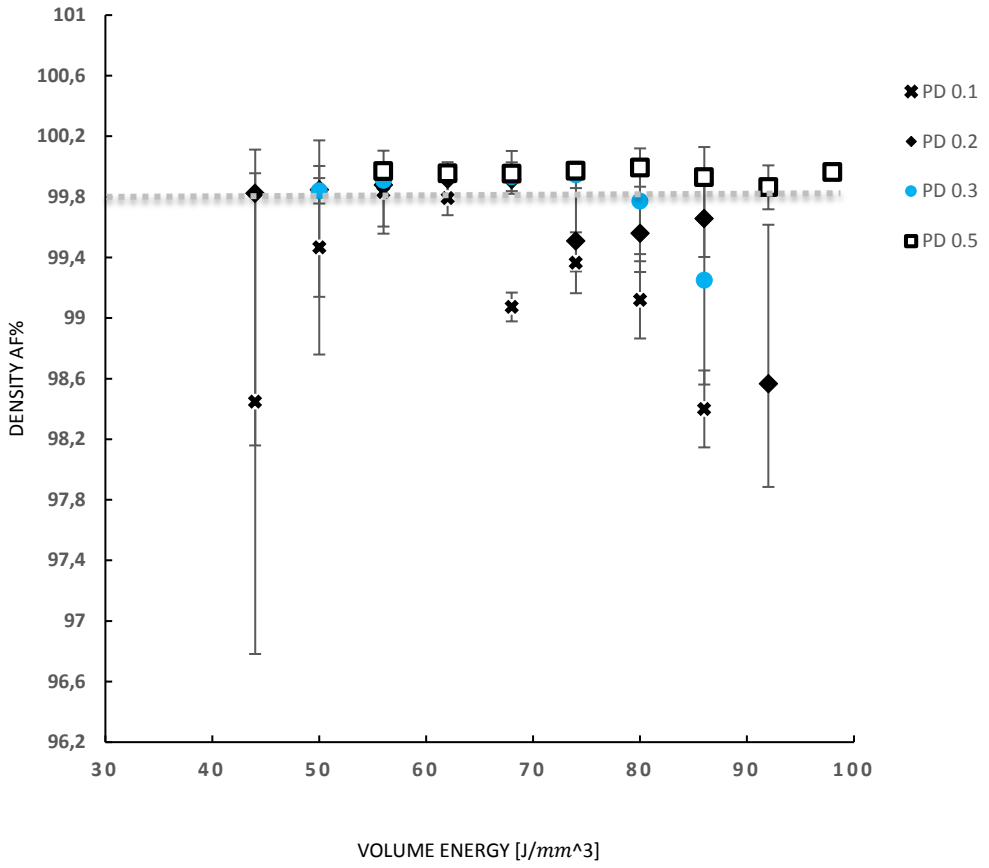

Figure 4.6 Graph of total porosity as function of volume energy with varying point distance.

4.3.3 Investigation of a new type of porosity

The porosity measurements done in section 4.3.1 are including all types of porosity without clear differentiation between them. Figure 4.7a and b illustrate the appearance of a new type of porosity that occurs at higher volume energy in the process window after dense specimens are achieved. This means that this new type of porosity seems to appear at higher volume energies where traditionally only swelling should be occurring. It is also clear that there are specimens with the new type of porosity with no geometrical signs of swelling on the sidewalls. The new type of porosity will be referred to as "Beam induced porosity" (BIP).

Figure 4.7a and b provide overview images of what appears to be BIP (marked with black box) porosity at 25X magnification. The frequency at which the BIP starts to appear is increased at higher volume energy with constant point distance. The same trend is observed in specimens from other build plates although it is more apparent in specimens with point distance of 0.1mm compared to specimens with larger point distance and spot time.

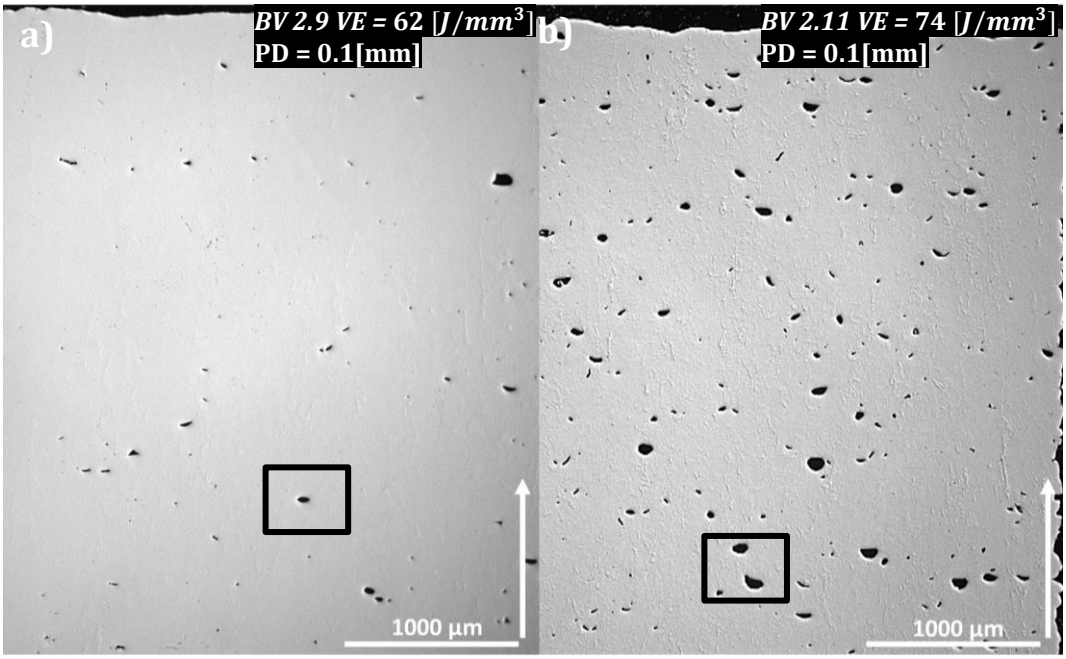

Figure 4.7 Optical micrographs of BIP at 25X magnification ***a)*** *Minor amounts of BIP* ***b)*** *Severe amount of BIP.*

Figure 4.8a and b show a comparison of the occurrence of BIP (marked with black box) in specimens with the same point distance but different volume energies. Specimen BV2.9 can be identified as the onset of BIP, which means that specimens at volume energies below that of BV2.9 do not show the occurrence of BIP. The difference between Figure 4.8a and b are the more frequent occurrence in the latter. It is important to note that Figure 4.8b is located higher up in the process window with higher volume energy input.

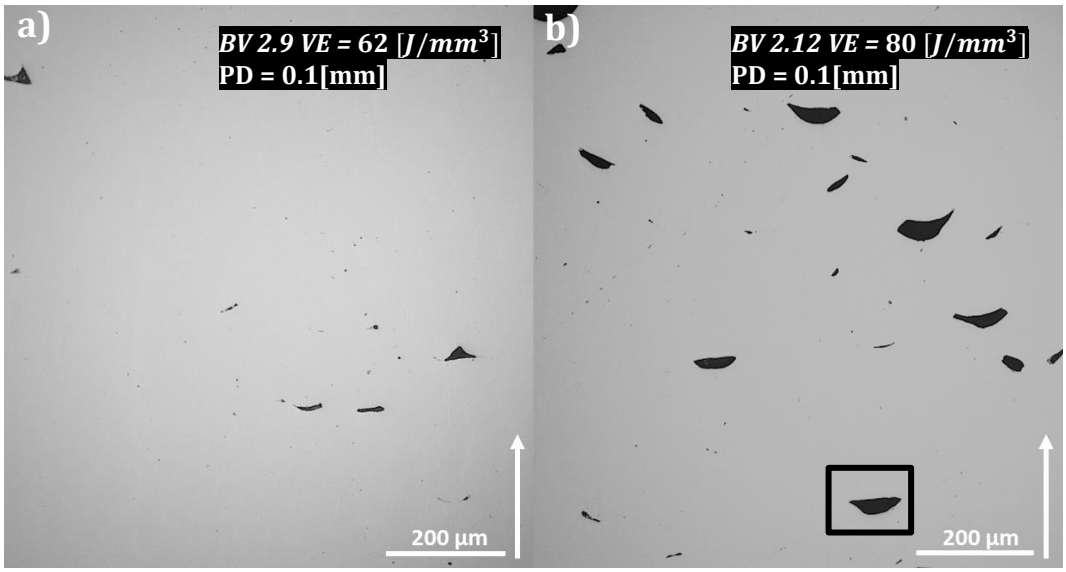

Figure 4.8 BIP at 100X magnification in specimens with same point distance but difference volume energy input ***a)*** *Low volume energy, small amount of BIP visible* ***b)*** *High volume energy, large amount of BIP visible.*

Figure 4.9a and b illustrate the BIP (marked with black box) in specimens with point distance of 0.3 mm as compared to previous images in Figure 4.8 with point

distance of 0.1 mm. Figure 4.9c and d provide an impression of the shape of the new type of pores. The BIP in Figure 4.9 is larger than those in Figure 4.8. The shape also varies as the BIP in the Figure 4.9 is more elongated in the build direction while the BIP in Figure 4.8 is thinner (plate-like) along the build direction.

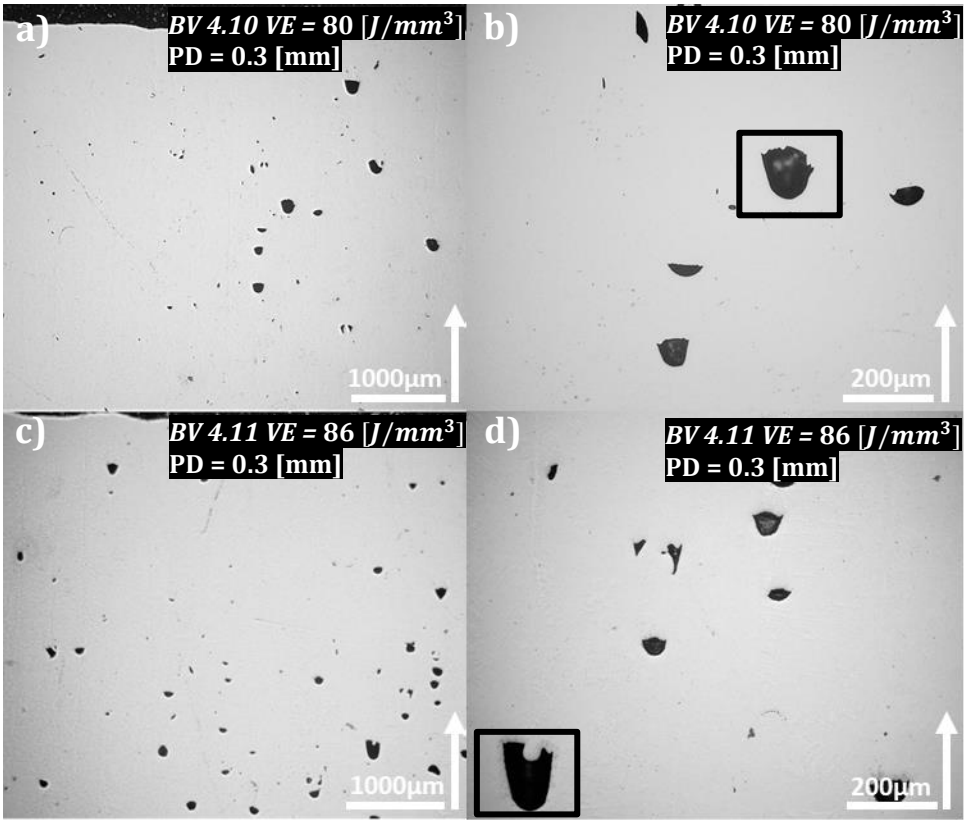

*Figure 4.9 Appearance of BIP in specimens with larger point distance **a)** 25X magnification **b)** 100X magnification **c)** 25X magnification **d)** 100X magnification.*

4.3.4 Identification of specimens having BIP

Specimens indicating severe amount of BIP are identified in order to locate the location of BIP in the process window with regards to volume energy and point distance. Specimens in Table 6 were further investigated and those showing BIP were marked. The specimens indicating appearance of BIP are marked in Table 7. This enables quantification of fraction of the BIP as part of the total amount of porosity (TAP).

- T indicates typical porosity (Lack of fusion and gas porosity).
- O Indicates onset of BIP porosity.
- X indicates severe amounts of BIP porosity.

Table 7: BIP identification

BV2	**5**	**6**	**7**	**8**	**9**	**10**	**11**	**12**	**13**
PD = 0.1mm	**T**	**T**	**T**	**T**	**X**	**X**	**X**	**X**	**X**
BV1	5	6	7	8	9	10	11	12	13
PD = 0.2mm	**T**	**T**	**T**	**T**	**O**	**X**	**X**	**X**	**X**
BV4	5	6	7	8	9	10	11	12	13
PD = 0.3mm	**T**	**T**	**T**	**T**	**O**	**X**	**X**	**-**	**-**
BV3	5	6	7	8	9	10	11	12	13
PD = 0.5mm	**T**	**T**	**T**	**T**	**T**	**T**	**O**	**O**	**-**
BV5	6	8	9	10	11	12	13	14	15
PD = 0.5mm	**-**	**-**	**-**	**-**	**-**	**-**	**-**	**-**	**T**

Black arrow indicates higher volume energy direction.
PD = point distance.
-Specimen not tested/phased out in previous categorization step.

4.3.5 BIP porosity quantification

BIP was manually removed from the images with help of the ImageJ software as shown on in Figure 4.10. The porosity excluding BIP was measured to quantify the fraction of BIP of total amount of porosity.

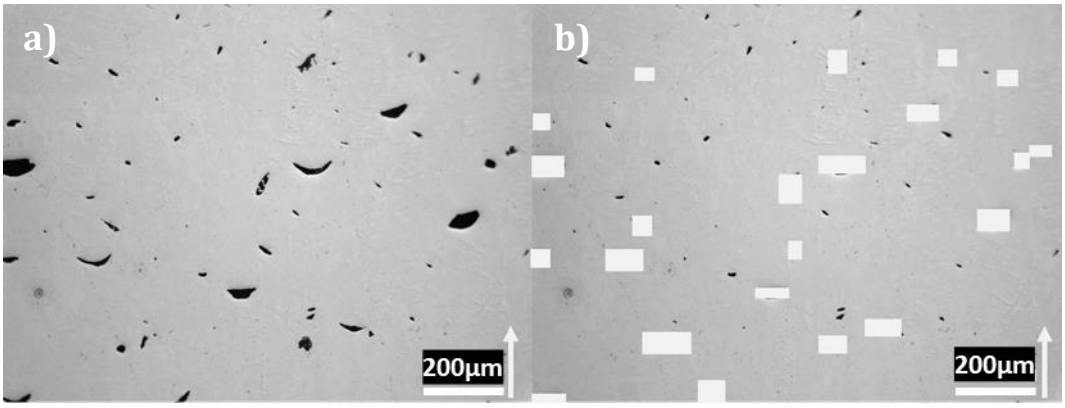

*Figure 4.10 BIP porosity removal **a)** Original image captured showing BIP **b)** Image after manual removal of BIP.*

As can be seen in Table 8, the BIP contribution is the difference between what would be a dense specimen and a porous. Besides specimen BV2.10 all specimens are dense if BIP is excluded from total amount of porosity (TAP).

- T indicates typical porosity (lack of fusion and gas porosity).
- O Indicates onset of BIP porosity (not possible to see a clear volume energy at which BIP appears in some specimens).
- X indicates severe amounts of BIP porosity.

Table 8 Quantification of BIP and TAP (Total amount of porosity) porosity.

Specimen series BV1	**5**	**6**	**7**	**8**	**9**	**10**	**11**	**12**	**13**
Type	T	T	T	T	**X**	**X**	**X**	**X**	**X**
TAP %	T	T	T	T	0.09	0.49	0.44	0.34	1.43
Excluding BIP %	T	T	T	T	0.02	0.03	0.09	0.03	0.08

Specimen series BV2	**5**	**6**	**7**	**8**	**9**	**10**	**11**	**12**	**13**
Type	T	T	T	T	**O**	**X**	**X**	**X**	**X**
TAP%	T	T	T	T	0.21	0.93	0.64	0.88	1.6
Excluding BIP %	T	T	T	T	0.14	0.22	0.11	0.13	0.17

Specimen series BV3	**5**	**6**	**7**	**8**	**9**	**10**	**11**	**12**	**13**
Type	T	T	T	T	T	T	**O**	**O**	-
TAP%	T	T	T	T	T	T	0.14	0.04	-
Excluding BIP %	T	T	T	T	T	T	0.01	0.02	-

Specimen series BV4	**5**	**6**	**7**	**8**	**9**	**10**	**11**	**12**	**13**
Type	T	T	T	T	**O**	**X**	**X**	-	-
TAP%	T	T	T	T	0.06	0.23	0.75	-	-
Excluding BIP %	T	T	T	T	0.03	0.1	0.12	-	-

Specimen series BV5	**6**	**8**	**9**	**10**	**11**	**12**	**13**	**14**	**15**
Type	-	-	-	-	-	-	-	-	T
TAP%	-	-	-	-	-	-	-	-	T
Excluding BIP %	-	-	-	-	-	-	-	-	T

-Specimen not tested/Phased out in previous categorization step.

4.4 Process window including BIP

A second process window is obtained where differentiation is made between different types of porosity. The specimens marked as dense in the primary process window are now divided into two categories “Dense” and “BIP”. A trend relating appearance of BIP higher up in the process window at smaller point distances can be seen. Specimens indicating severe amounts of BIP are highlighted with a boarder as seen in Figure 4.11. The largest point distance of 0.5 result in most dense specimens.

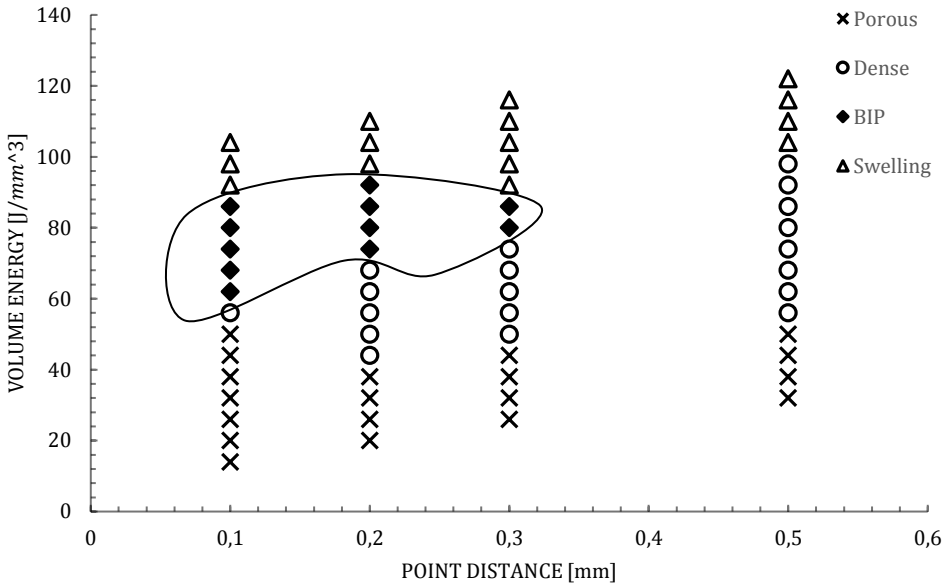

Figure 4.11 Second process window including BIP and its location with regards to volume energy.

4.5 Melt pool characteristics

To be able to define the depth of the melt pool, images are captured at each different point distance just below the melt surface. The melt pool is most clearly visible on the last melted layer as there is no subsequent re-melting compared to layers further down in the specimens which are affected by a repeating cyclic reheating of subsequent layers.

The point distance influences the width of the melt pool as can be seen in Figure 4.12a-d. With increasing point distance at constant volume energy of 56 [J/mm^3] the melt pool appears to have an increasing width illustrated with a black line in Figure 4.12 a-d. As the point distance increases, the number of points is decreasing, and the spot time is increasing. This means that given constant volume energy, the specimen with largest point distance will have much fewer points but at the same time longer spot time which leads to longer exposure to electrons hitting the area that is being melted compared to smaller point distances.

The melt pool depth is not always easy to observe as compared to the width. It can be said that given constant volume energy input the specimens with larger point distance seem to have a deeper melt pool. This can be seen as the number of visible layers are decreasing as the point distance increases. Comparing Figure 4.12a and d, the first image does show many non-ordered layers of re-melted powder while Figure 4.12d does show three layers of more organized re-melted layers but as stated earlier it is not always easy to see.

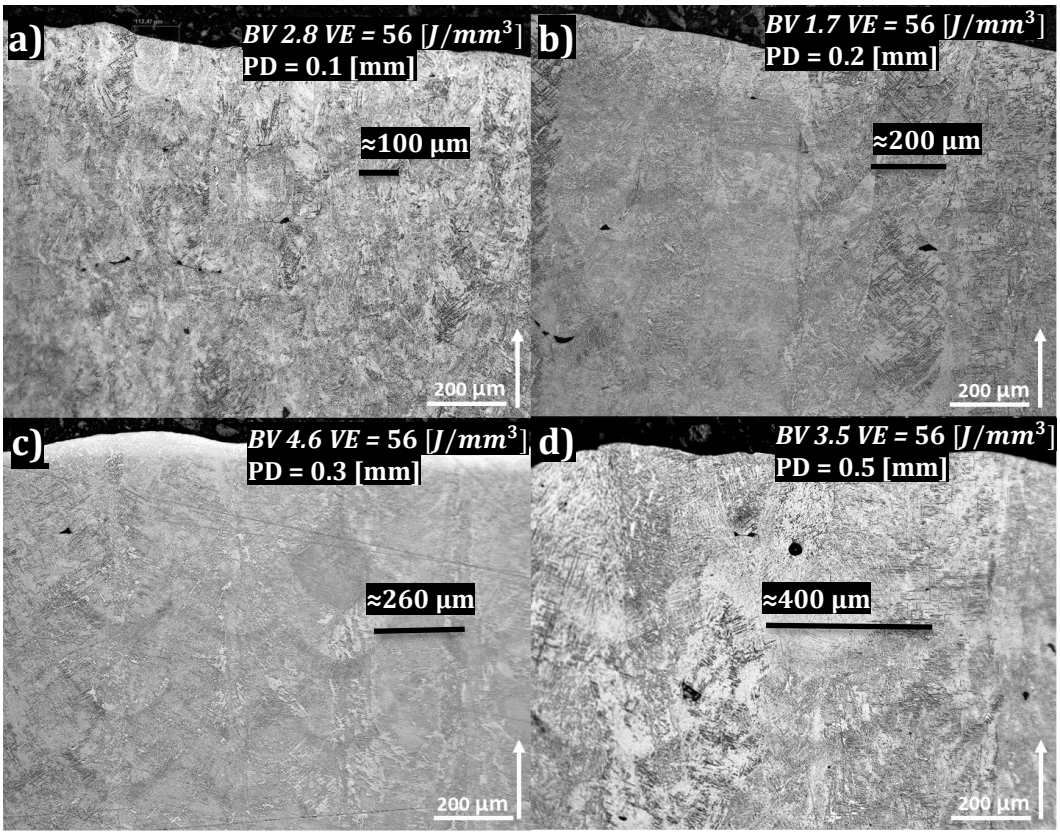

Figure 4.12 Size of pool depth and width in specimens with increasing point distance at constant volume energy input ***a)*** *Small melt pool width* ***b)*** *Melt pool width increasing with point distance* ***c)*** *larger melt pool width as the point distance increases* ***d)*** *The largest melt pool width is observed with the largest point distance at constant volume energy.*

4.5.1 Melt pool characteristics with constant point distance and increasing volume energy input

Figure 4.13a and b show the effect of increasing volume energy at constant point distance on the melt pool. Figure 4.13b does show a much deeper melt pool of ≈1000 µm compared to Figure 4.13a where the depth is ≈360 µm. The melt pool depth is illustrated by the vertical black arrows in the images. In Figure 4.13a, several layers can be observed while in Figure 4.13b only one layer can be observed throughout the whole length of the image along build direction. However, the melt pool width seems not to be affected drastically with increasing volume energy as the horizontal black arrows indicate.

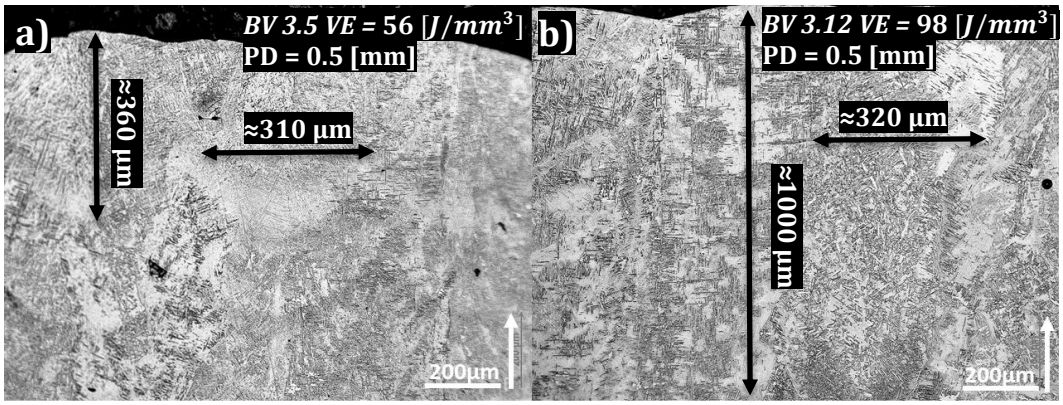

*Figure 4.13 Characterization of melt pool depth and width in specimens produced with **a)** Low volume energy **b)** High volume energy.*

4.6 Microstructural observations along build direction

4.6.1 Macro-level observations

The overview images at 25X magnification show a clear trend of non-order to ordered structure of the point structure. The larger the point distance the more ordered structure of the point order is visible. Figure 4.14a shows the least ordered structure while as the point distance increases, there are more distinct columns growing along the build direction. These columns of points (melt pools) are visible especially in Figure 4.14b-d while in Figure 4.14a it is not as clear to see ordered columns of points growing along the build direction. The volume energy input is at 56 [J/mm^3] for all for specimens.

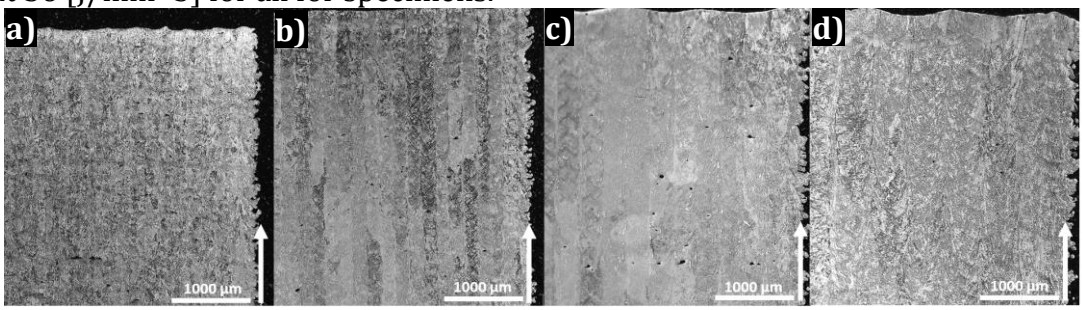

*Figure 4.14 Evolution of the point structure with varying point distance along the build direction illustrated by the white arrow **a)**Non-ordered structure, PD = 0.1mm **b)** Ordered structure, PD = 0.2 mm **c)** Ordered structure, PD = 0.3 mm **d)** Ordered structure, PD = 0.5mm.*

4.6.2 Microstructure evolution with location

As seen in Figure 4.15a and b there is a substantial difference between different parts of the specimens. The bottom part is exposed for a longer time to high temperatures compared to areas close to the surface. At the bottom of the specimens, an aged structure is found, compared to the surface of the specimens.

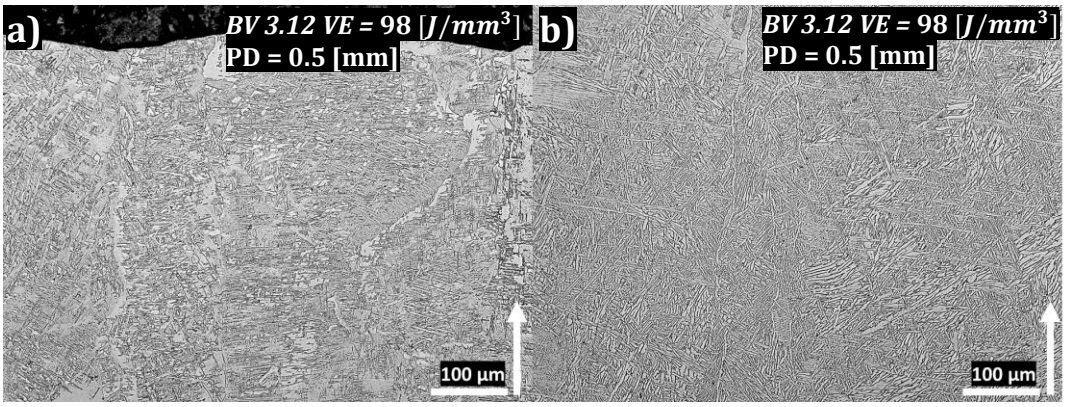

Figure 4.15 Microstructure variation at different locations in the specimen ***a)*** *Image captured just below last melted layer. Fine* $\alpha + \beta$ *structure is observed.* ***b)*** *Image captured at the bottom part of the specimen close to the support structure. Aged* $\alpha + \beta$ *structure is observed.*

At higher magnification it is possible to observe the difference in microstructure in more detail as shown in Figure 4.16a-b. Just below the surface, a finer structure with a high amount of what looks like as acicular martensitic α′ is observed. The lower parts of the specimen remind more of an aged coarse Widmanstätten structure.

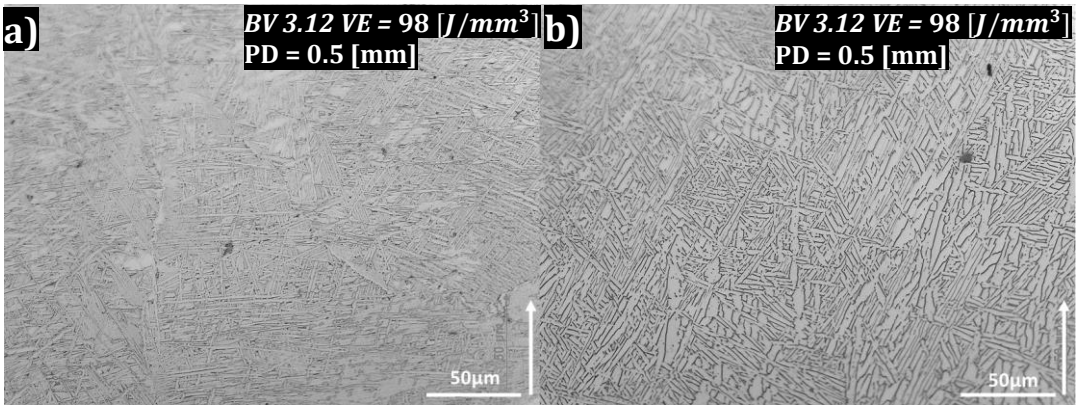

Figure 4.16 Different aging time effect on the microstructure ***a)*** *Below last melted layer, possible α′ structure is visible* ***b)*** *Bottom part of the specimen close to the support structure,* $\alpha + \beta$ *structure is observed.*

Within each build plate series, with increasing volume energy at constant point distance, it is possible to observe coarser microstructure in the specimens with higher volume energy input since the higher volume energy leads to larger melt pools and thereby to a slower cooling rate [31]. This results in a microstructure which is coarser as shown in Figure 4.17b compared to Figure 4.17a. Figure 4.17a shows a more Basketweave microstructure compared to Figure 4.17b where a more Widmanstätten microstructure is observed due to slower cooling rate [27]. Figure 4.17b shows more equiaxed structure inside the previous β grains as can be explained by more diffusion and less nucleation compared to Figure 4.17a [27] [32].

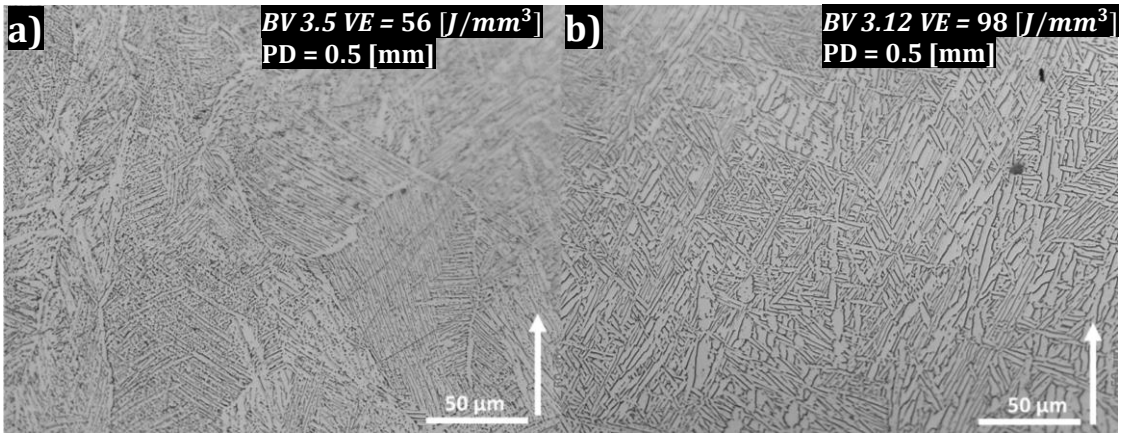

Figure 4.17 Microstructure evolution with different volume energy input given constant point distance ***a)*** *Close to support structure, fine α + β microstructure* ***b)*** *Close to support structure, coarse α + β microstructure observed.*

Figure 4.18a-d illustrates the evolution of microstructure with varying point distance and constant volume energy. Figure 4.18a shows clear signs of α on previous β grain boundaries in long white stripes. As the point distance increases it is more difficult to observe the grain boundaries. It is also difficult to observe any trends regarding the size and morphology of the $\alpha + \beta$ microstructure as the point distance is increased.

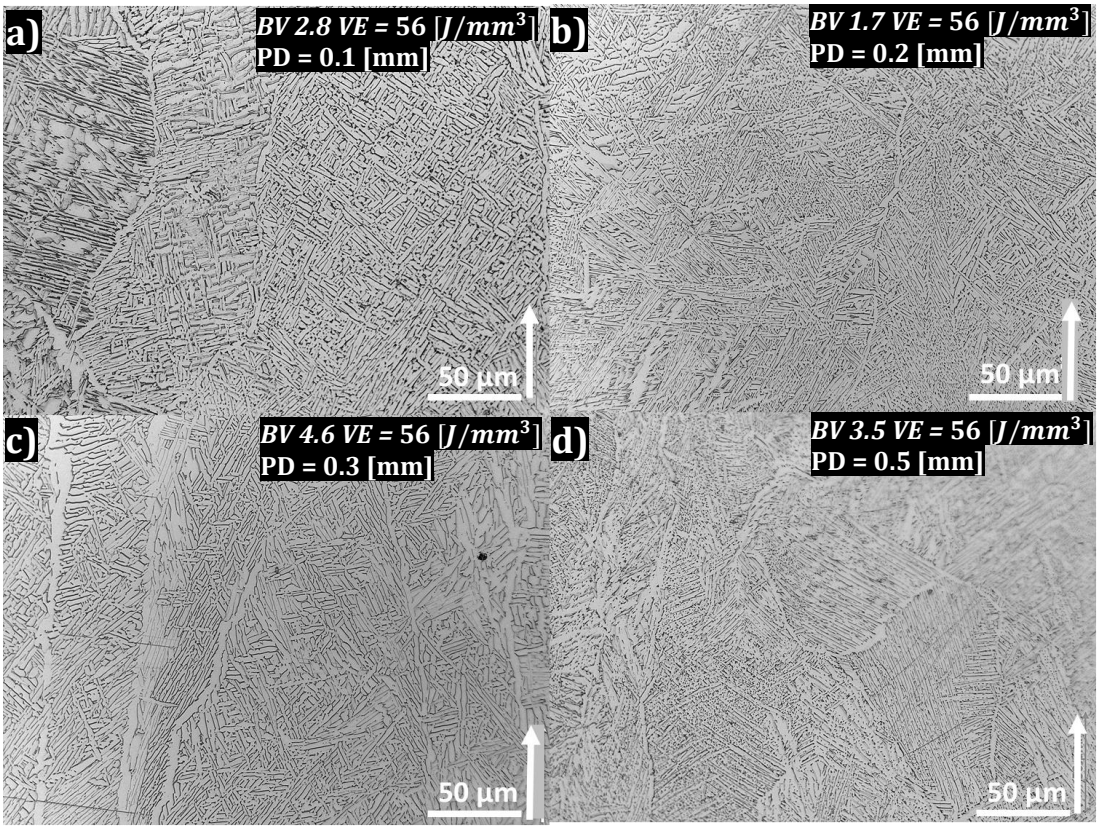

Figure 4.18 Evolution of the α + β microstructure with varying point distance given constant volume energy input, all four images captured close to the support structure ***a)*** *Visible grains boundaries with coarse α + β structure* ***b)*** *Fine α + β structure* ***c)*** *Coarse α + β structure* ***d)*** Fine $\alpha + \beta$ structure.

To illustrate the point structure in the different specimens, images are captured at 25 times magnification, see Figure 4.14. As can be seen in Figure 4.19, the specimen with smallest point distance has a more observable grain structure and as the point distance increases it's more difficult to identify the grains. Figure 4.19a shows no clear sign of texture along the build direction.

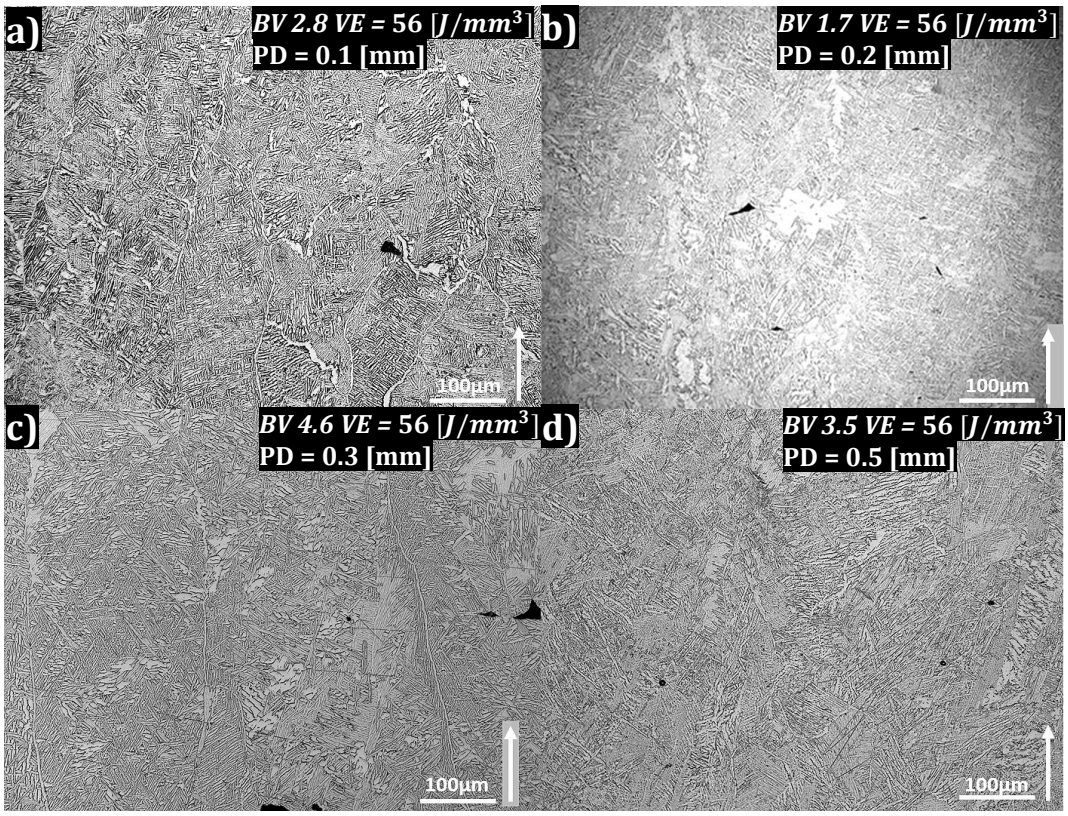

*Figure 4.19 Grain structure variation with varying point distance given constant volume energy input **a)** Multiple smaller grains visible, clear indication of α on grain boundaries **b)**Non-visible grains structure, α + β structure visible throughout the image **c)** Non-visible grains structure, α + β structure visible throughout the image **d)** Non-visible grains structure, α + β structure visible throughout the image.*

4.7 Hardness indentation test

The hardness measured on specimens with different point distances is illustrated in Figure 4.20a-d. At constant point distance the hardness decreases with increasing volume energy. This behaviour is observed for all four different point distances. Hardness values obtained from specimen BV2.5 with point distance of 0.1 mm are not viable as this is a porous specimen. As the indentation hits a porous area, unreliable results are generated. There is a slight trend most clearly seen in Figure 4.14c, for the two highest volume energy inputs were the hardness increases as the indentations get closer to the surface of the specimen. In general, the hardness is comparable or slightly higher than the hardness observed in specimens with traditional hatch strategy (depending on volume energy input and point distance).

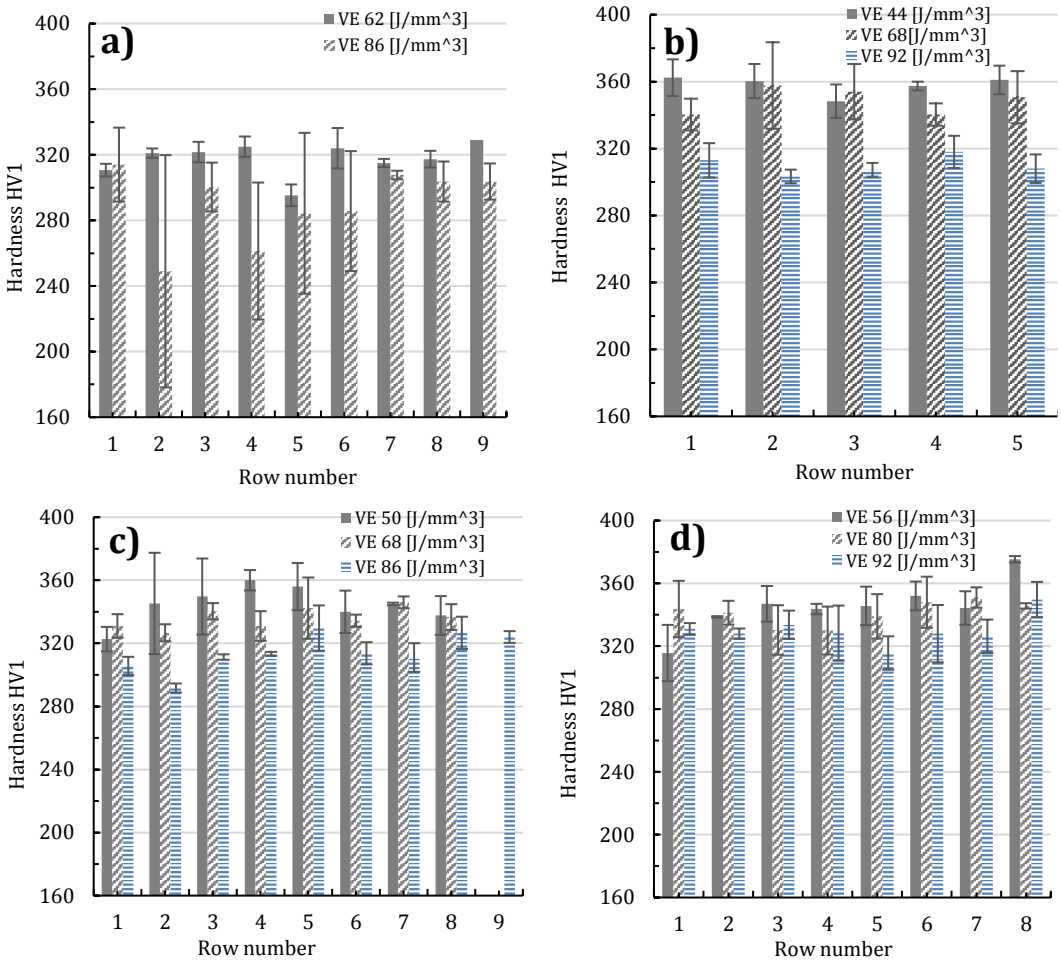

Figure 4.20 Measured hardness in different specimens with varying point distances and volume energies: ***a)*** *0.1 mm* ***b)*** *0.2 mm* ***c)*** *0.3 mm* ***d)*** *0.5 mm.*

5 Discussion

5.1 General porosity

Point melting strategy does show similar occurrence of lack of fusion defects at low energy input across all specimens belonging to different process setups with varying process parameters. This results in uncomplete melting of powder particles approximately up to volume energies of 35- 60 J/mm^3 depending on point distance as seen in the primary process window in Figure 4.3. The presence of gas porosities is also seen in traditional hatch scanning strategy, as seen in Figure 4.4. The difference starts to appear as the new type of porosity (BIP) start to appear especially in specimens with short spot time and small point distance as seen in the second process window including BIP in Figure 4.11.

With a few exceptions that could be due to experimental inaccuracies, in the specimen preparation process and image processing in the ImageJ software it is possible to observe higher specimen density at constant volume energy with increasing point distance (as seen in Figure 4.6). This has implication for the size

of the melt pool as the point distance increases and thereby spot time and means that if the objective is to find the least amount of porosity then longer spot time and larger volume energy is wanted. However, the microstructure is affected since larger melt pools can lead to slower cooling rates and in general larger grains and coarser structure inside each grain as seen in Figure 4.17 [31]. Therefore, it is important to find a balance between parameters such point distance, volume energy and spot time.

5.2 Appearance of BIP

As the volume energy increases beyond the threshold where fully dense material is obtained, we start to see the occurrence of this new kind of porosity. Traditionally, as the energy input increases, the process should involve three stages of specimen integrity as shown in Figure 5.3. Lack of fusion dominates at lower volume energy as seen in Figure 5.1a. As the energy input increases, as seen on Figure 5.1b, dense specimens are achieved. At even higher volume energy BIP starts to appear as seen in Figure 5.1c and in Figure 5.1d severe amounts of BIP is observed. Figure 5.1a and d have approximately same amount of porosity of 1.6%, but it can clearly be observed that in Figure 5.1a lack of fusion dominates, while in Figure 5.1d BIP is the main reason for the porosity. This trend is observed for all the different build plates with different parameters. The onset of the BIP in regard to volume energy seems to vary with spot time. As seen in the second process window in Figure 4.11, BIP starts to appear more frequently at smaller point distances and given constant point distance BIP appears at higher volume energies. All specimens besides one showing BIP do also show that BIP is a major factor in regard to the amount of porosity measured. These specimens would be regarded as dense (< 0.2% Af porosity) once BIP is removed as fraction of total amount of porosity as seen in Table 8. It is important to quantify when and where BIP appears and to what extent for future studies if the reason behind BIP is a hardware limitation as explained earlier in section 3.1.4. This could lead to that future machines might be able to perform better regarding BIP.

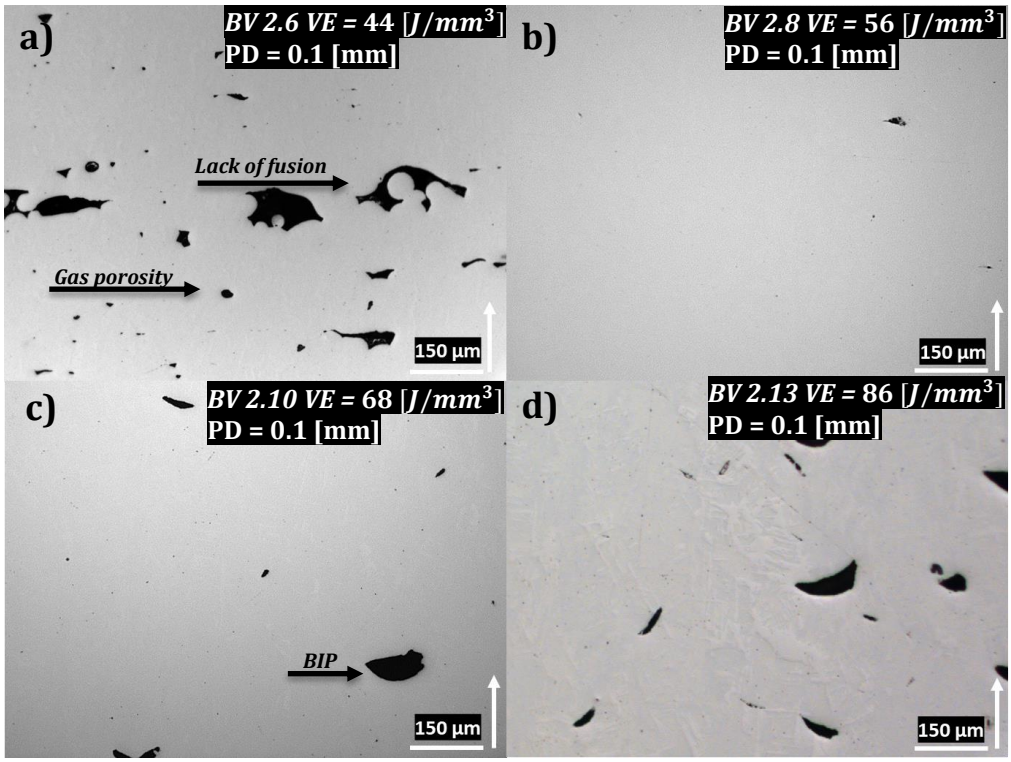

Figure 5.1 Evolution of specimen quality as the volume energy input increases ***a)*** *Lack of fusion dominates* ***b)*** *Dense specimen* ***c)*** *Onset of BIP defects* ***d)*** *BIP dominates.*

It is more difficult to find out which of the parameters, point distance and volume energy, are more directly related to appearance of BIP. It can be observed that BIP appears less frequently when comparing specimens with constant volume energy and increasing point distance. At the same time, it is also observed that BIP increases at constant point distance with increasing volume energy. This study gives an indication that spot time might be the more important parameter to investigate further as the second process window does indeed show that the smallest point distance results in significant amounts of BIP containing specimens while the larger point distance does not lead to as many specimens with BIP. This would suggest that fewer points and longer spot time would also be of benefit to avoid BIP as the point distance increase. However, to find out which parameter affects the occurrence of BIP more, future studies need to be focused on the rate at which BIP appears as parameters vary.

Since BIP can be a significant fraction of the porosity measured a porosity measurement excluding BIP is shown in Figure 5.2. The measurement is done in specimens showing BIP defects as explained in section 4.3.5. As can be seen, all specimens except one are dense (below the horizontal black dotted line) if BIP is excluded. Due to the significance of BIP in regard to obtained density at high volume energy it can be said that there is a need for future improvements in the hardware.

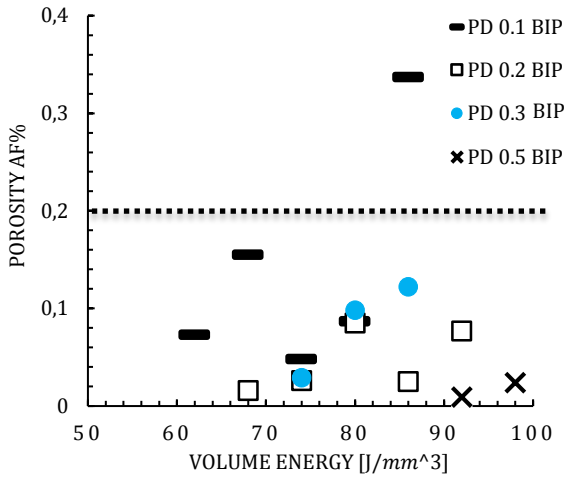

*Figure 5.2 Measured porosity if BIP is excluded in specimens suffering from BIP. * Black line illustrates the 0.2% porosity fraction*

5.2.1 BIP relation to swelling

In traditional hatch scanning strategies, only swelling should be visible at higher volume energy but the point melting strategy results in occurrence of BIP in addition to swelling. The BIP always show similar morphology. The only difference is the size of the BIP which is varying depending on spot time and point distance. An interesting observation is that in some specimens there is evidence of onset of BIP before swelling is visible. This can be seen in some specimens being considered "dense" and without showing swelling in the primary process window. Further investigations by optical microscopy indicated occurrence of BIP in these specimens. This indicates that BIP does not need to be directly related to swelling. This study did not differentiate further between those two scenarios as specimens indicating swelling defects were already phased out before porosity measurements were performed. However, it is of importance to be aware of this phenomenon for future studies and see if BIP appears even more frequently in specimens showing swelling.

In the Figure 5.3a and b the possible difference between traditional hatch scanning and point melting is illustrated. At low to medium volume energy input the defects appearing in point melting is similar to the traditional hatch scan strategy. The difference in type of defects appearing between the two scanning strategies appears at high volume energy inputs as seen in Figure 5.3. There is need for more data to back up any hypothesis, but the idea is nonetheless interesting to explore as the shape of the BIP is something that is not seen in traditional hatch scanning strategy. This study manages to suggest that such porosity exists, but more data is needed to draw a broader conclusion regarding BIP.

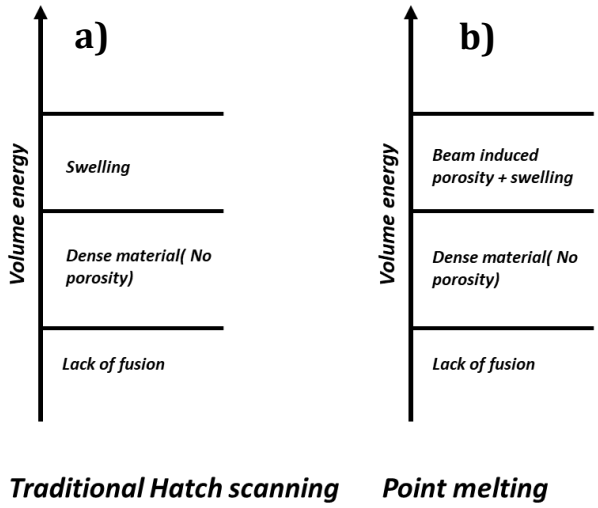

Figure 5.3 Different defect types in hatch scanning and point melting with increasing volume energy.

5.3 Frequency of BIP

The frequency at which the BIP starts to appear seems to have a correlation with the number of melt points and an inverse relation with spot time as seen in Figure 5.4. The arrow heads in the figure indicate the increase of the parameters. The dashed black arrow indicates the build direction. As the spot time decreases, it is more difficult for the hardware to control the focus and de-focus cycles of the beam. As the spot time gets smaller, the control of the beam becomes a more substantial limitation. The positional accuracy of the beam could also depend on the spot time since longer spot times give more room for adjusting the desired location of the beam. The shorter spot time could also affect the accuracy of beam power output. As the machine operates at a smaller spot time there is less time left for the machine to have an accurate output of wanted beam current. Comparing the smallest point distance (0.1mm) to the largest (0.5mm) given constant volume energy input, the difference in point distance is 5 times while the spot time difference is 25 times. This means that for the same wanted beam output there is 25 times more time to make sure that an accurate control of the beam is achieved while working on the larger spot time. It can be hypothesized that the smaller spot time creates an environment where the beam current can be too high as the melting process begins and thereby this can lead to excessive amounts of material being melted and create porosity. At the same time if the beam power output is below the desired value, less than optimum amount of powder might be melt and hence the BIP porosity appears.

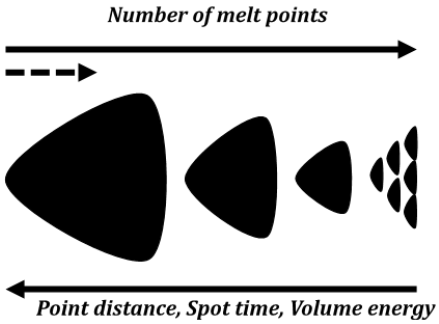

Figure 5.4 Parameters relation to BIP, as the point distance increases the number of points decreases. BIP appears as larger in size but fewer in numbers at larger point distance compared to smaller point distances.

5.4 Microstructural observations

5.4.1 Spot time and relation to microstructure

As stated in section 3.1.4, the smallest possible spot time is a hardware limitation which is possible to improve. As the spot time and point distance decreases, so does the size of the melt pool as seen in *Figure 4.12*. A decrease in melt pool size results in an increase in cooling rate which affects the amount of undercooling and the obtained microstructure. The faster the cooling rate the finer microstructure and better effect of the Hall-Petch effect can be obtained regarding hardness.

5.4.2 Volume energy effect

The melt pool depth depends on volume energy input at constant point distant. As can be seen in Figure 4.13, the depth of the melt pool increases with volume energy although the width of the melt pool seems not to change noticeably. The deeper the melt pool the more of the previous layers are exposed to higher temperatures which could possibly lead to better interlayer cohesion as several layers are re-melted again. It could also indicate a more aged structure, but this cannot be backed-up by data in this work. Another effect of the depth of the melt pool can be its role in the occurrence of the BIP. As seen in Figure 4.11, the specimens with smaller point distance seems to be much more affected by BIP than the specimens with larger point distances. The depth of the melt pool could affect the BIP when it is created, i.e. as the melt pools becomes deeper, the BIPs that were created in previous layers might be re-melted. Hence, large point distance and larger volume energy input could be favourable in regard to BIP appearance.

As the energy density increases given all other parameters being constant, more of the previous layers is remelted and the deeper the remelting is. This leads to larger and more interlayer melting and coarser microstructure. Since titanium has very low thermal conductivity, 7 W/m at room temperature, this could increase the effect of increasing grain size at overlapping areas between the different melt pools [33].

A comparison is made between the two dense specimens with largest difference in volume energy. It can clearly be observed that the specimen in Figure 5.5a shows a much finer microstructure compared to the specimen in Figure 5.5b. The coarser structure in Figure 5.5b can be explained by longer spot time and larger melt pool which would decrease the cooling rate. Slower cooling rates enables

more diffusional transformation of β into α + β and less martensitic transformation of β into α′. Figure 5.5a shows clear indication of what could be α phase (white colour) on previous β-grain boundary.

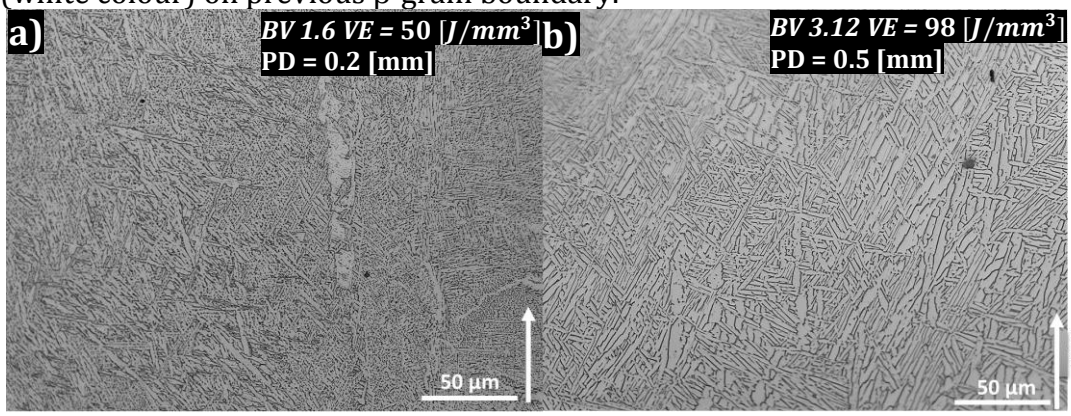

Figure 5.5 Comparison of microstructure in specimens with the largest difference in volume energy input resulting in dense specimen, images captured at the bottom part of the specimens close to the support structure ***a)*** *Fine structure of α + β* ***b)*** *Coarse structure of α + β.*

Figure 4.17 shows that larger volume energy input also leads to coarser microstructure with constant point distance. Figure 5.5b shows a clear indication that the microstructure appears to evolve to a coarser structure due to the larger volume energy input even at varying point distance. Looking at Figure 4.18 it is not as clear to observe any trends when comparing specimens at constant volume energy and increasing point distance. In theory, the specimen with larger point distance hence larger melt pool should indicate a coarser microstructure due to slower cooling rate. Specimens with the smallest point distances should have the finest microstructure due to smaller melt pool and faster cooling rate. But it is not possible to back-up this hypothesis with the data obtained in this work in regard to constant volume energy and varying point distance.

5.4.3 Grain structure

Figure 4.19a shows the microstructure of the only specimen with density exceeding 99.8% when using the point distance of 0.1mm. There is a clear indication that the grain structure is not elongated along the build direction as it is in the traditional hatch scanning. Even though it is more difficult to observe grains when using larger point distances, there is still no columnar growth along the build direction as compared to traditional hatch strategy where columns of several hundred micrometres in length are found [1].

As shown in Figure 4.14, the smallest point distance of 0.1 mm provides the least ordered point structure. More points (melt pools) are observed while the order at which these points shape up along the build direction is less ordered as compared to larger point distances where an increasingly column-like structure is observed. Figure 4.14a with point distance of 0.5 mm clearly shows that the point structure (melt pools) does look like a column growing along the build direction, while Figure 4.14d shows a non-ordered structure of the point structure (melt pools).

5.4.4 Effect of point distance on microstructure

Point distance seem to affect the width of the previous β grains, as can be seen in Figure 4.19. Larger point distance could lead to larger previous β grains in which the α + β microstructure will grow inside. α grows at first on the previous β grain boundaries. Inside the grains, there is variety of different morphologies of α + β structures from Widmanstätten to basketweave structure as seen in Figure 4.17 and Figure 4.18. The difference between Widmanstätten and basketweave structures are difficult to observe in this work. The Widmanstätten structure seems to appear at slightly lower cooling rates while the basketweave structure seems to appear at slightly higher cooling rates [27]. At even higher cooling rates the martensitic α′ => α + β phase transformation should be possible to observe. However, since all specimens are aged at about 670 °C, the α′is most probably transformed into α and α + β.

5.5 Hardness

The hardness decreases with increasing volume energy at constant point distance. This behaviour is observed across all four specimen groups belonging to different build plates and thereby different point distance. This behaviour could be explained by the fact that as the point distance increases and fewer amount of points are melted per powder layer, larger melt pools are created as the spot time increase at the same time. Larger melt pools lead to slower cooling rate and thereby, as explained in Figure 2.4, more diffusional transformation occurs rather than nucleation of new grains [31]. Fewer grains would according to the Hall-Petch relationship lead to a decreasing hardness. Indications of an existing hardness gradient appears as the indentations are closer to the specimen surface. However, based on the results obtained in this project no broader conclusion can be drawn regarding a possible hardness gradient along the build direction.

5.6 Outlook for future studies

In future studies, it could be of interest to perform volumetric porosity measurements and investigate possible trends regarding the different kind of porosities and location of appearance. This could also be further used to have a more precise measurement of porosity as measurements in this work indicate a large spread in estimated porosity which varies greatly depending on location.

EBSD analysis could be performed in order to have a better understanding of the grain structure. While images captured by the optical microscope are a good basis to show the difference between traditional hatch strategy where columnar grains are observed and the new point melt strategy tried in this project, it is difficult to get a more detailed understanding based solely on images captured by optical microscope.

Simulations of temperature in each point of the powder bed and its evolution as process parameters such as point distance, point energy, spot time and volume energy change could help to further understand the phase transformations that occur and help to better predict the microstructure outcome.

Mechanical properties should be more thoroughly investigated based on fraction of α and β phase available in specimens at constant volume energy with different point distance. In addition to hardness testing, tensile drag testing should be performed. Comparison between specimens with point distance of 0.1 and 0.5 mm are of interest in order to specify possible improvements.

No in-depth hardness measurement is performed where specimens of two different point distances are compared to each other with the same volume energy. This would facilitate better understanding of the hardness and its relation to point distance. Based on the results obtained in this study, a possible trend is observed that indicates an increase in hardness as the indentations are farther away from the bottom of the specimen and closer to the specimen surface. This can be explained by the longer amount of time spent at aging temperature in the layers closer to the bottom of the specimen.

Less textured specimens might be achievable as the point structure is less ordered as discussed in section 4.6.1. By varying the point melt strategy between each powder layer more variation in the melt pools is possible to achieve. Today the point melt strategy is the same throughout all layers which means that point 1 is always at the same location in the point order and the only change is in the height (build direction). In future studies, in order to mimic more disorder in the melt pools and point structures, a point melt order should be chosen where location of each point in the grid is varied between different layers. The order used in this project is according Figure 5.9a. The proposed new strategy would be a mix of the two where the first layer would follow the order shown in Figure 5.9a and the second layer would be according to Figure 5.9b. Other strategies that would lead to more random ordered melt pools would be of desire.

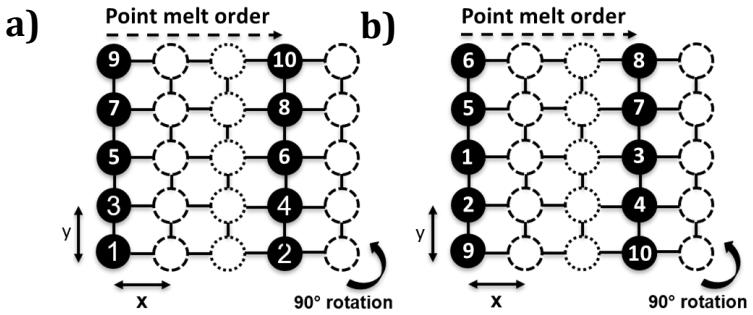

*Figure 5.9: Different point melt order strategies **a)** Point melt strategy used in this project **b)** Example of alternative point melt order.*

This work only focused on cubic specimens with the non-variable cross section area and shape. In order to have industrial utilization of point melting strategy, there is need for further studies with regard to cross-sectional changes and the challenges that arise as the parameters needs to be examined in regard to cross-sectional surface area changes.

More detailed investigations should be performed for this new scan strategy with respect to build rate. Comparison with the traditional hatch strategy will help in estimating the feasibility for industrial production.

An important aspect and reason for why efforts are put on to differentiate the type of porosities is the future development of the EBM machines. Improvements regarding smallest possible spot time, beam current and focus/de-focus time cycles could enable even smaller point distances without BIP. This could, theoretically, lead to denser and less textured specimens at the smaller point distances. Currently the Arcam Q10 machine produces only 1 dense specimen at point distance of 0.1 mm.

In order to better understand the reasons for BIP, it could be of interest to compare two sets of specimens at the smallest point distances produced with two different EBM machines. The variation between the machine accuracies at smaller point distance and spot times should be investigated in order to clearly understand if BIP is related to hardware limitations.

6 Conclusion

Porosity is increasing at smaller point distances given constant volume energy input. As the spot time, point distance decreases and volume energy increases, increasingly BIP looks to be the main reason behind the visible porosity as compared to the more traditional gas porosity and lack of fusion.

BIP appears at higher volume energy input in the process window.

BIP porosity appears more often at smaller point distance and spot time given constant volume energy.

Microstructures of dense specimens are mostly a combination of Widmanstätten and basketweave $\alpha + \beta$ structure with α on previous β-grain boundary and $\alpha + \beta$ structure inside the grains. Coarse structure is obtained at higher volume energies and finer structure is obtained at low volume energy input.

The microstructure varies with height as the last melted layers are aged for a shorter time at the build temperature of 670°C compared to layers close to the support structure.

Specimens produced with smaller point distance show more equiaxed and less elongated grains along the build direction compared to hatch strategy, where elongated grains along the build direction are obtained. less ordered structure of the melt pools is also observed as number of points increase with decreasing point distance.

Hardness is decreasing as the volume energy input increases due to larger melt pool and slower cooling rate.

Above mentioned conclusions led to a conclusive third and final process window as seen in Figure 6.1. The dashed contoured area shows where dense specimens are achieved. The region in the process window resulting in specimens showing BIP defects are also highlighted. The process window gives a first indication to what energy levels and point distances are required to achieve different properties and dense specimens. Parts requiring different microstructural properties can be achieved by choosing spot time and point distance together with volume energy input. It can shortly be concluded that denser specimens are achieved at the same volumetric energy input when using larger point distance and longer spot times. But at the same time this leads more textured microstructure and fewer but larger grains.

The point melting strategy in EBM enables tailored variable microstructure within a part by varying the point melt order during a build. This process opens the door for future AM-build parts with both textured and isotropic properties within the same part.

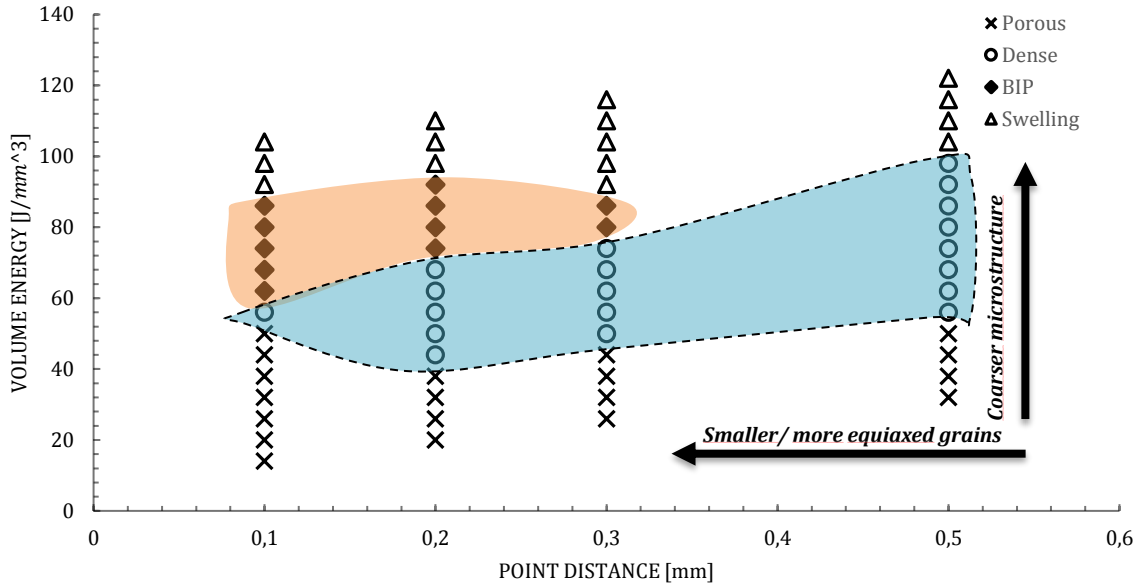

Figure 6.1 Final process window including microstructure properties. Dense specimens highlighted with dashed contour.

7 References

[1] A. Safdar, L. Y. Wei, A. Snis, and Z. Lai, “Evaluation of microstructural development in electron beam melted Ti-6Al-4V,” *Mater. Charact.*, vol. 65, no. Dld, pp. 8–15, 2012.

[2] A. Okello *et al.*, “Erratum to: Strategy for Texture Management in Metals Additive Manufacturing,” *JOM*, 2017.

[3] S. A. M. Tofail, E. P. Koumoulos, A. Bandyopadhyay, S. Bose, L. O’Donoghue, and C. Charitidis, “Additive manufacturing: scientific and technological challenges, market uptake and opportunities,” *Materials Today*. 2018.

[4] R. K. Ek, *Electron beam melting : Impact of part surface properties on metal fatigue and bone ingrowth*. 2019.

[5] A. Safdar, *A Study on Electron Beam Melted Ti-6Al-4V Division of Solid Mechanics Department of Construction Sciences*. 2012.

[6] M. Ramsperger and C. Körner, “Selective electron beam melting of the single crystalline nickel-base superalloy CMSX-4®: From columnar grains to a single crystal,” *Proc. Int. Symp. Superalloys*, vol. 2016-January, pp. 341–349, 2016.

[7] L. E. Murr *et al.*, “Fabrication of metal and alloy components by additive manufacturing: Examples of 3D materials science,” *J. Mater. Res. Technol.*, vol. 1, no. 1, pp. 42–54, 2012.

[8] Y. Zhai, H. Galarraga, and D. A. Lados, “Microstructure, static properties, and fatigue crack growth mechanisms in Ti-6Al-4V fabricated by additive manufacturing: LENS and EBM,” *Eng. Fail. Anal.*, vol. 69, pp. 3–14, Nov. 2016.

[9] H. Gruber, P. Karimi, E. Hryha, and L. Nyborg, “Effect of powder recycling on defect formation in electron beam melted Alloy 718,” *Powder Metall. Prog.*, vol. 18, no. 1, pp. 40–48, 2018.

[10] W. J. Sames, F. A. List, S. Pannala, R. R. Dehoff, and S. S. Babu, “The metallurgy and processing science of metal additive manufacturing,” *International Materials Reviews*. 2016.

[11] D. Bermudez, C. A. Terrazas, P. Morton, and R. Wicker, “Scanning Strategies in Electron Beam Melting To Influence Microstructure Development,” *Solid Free. Fabr. Symp.*, pp. 3–16, 2017.

[12] S. Tammas-Williams, H. Zhao, F. Léonard, F. Derguti, I. Todd, and P. B. Prangnell, “XCT analysis of the influence of melt strategies on defect population in Ti-6Al-4V components manufactured by Selective Electron Beam Melting,” *Mater.*

Charact., vol. 102, pp. 47–61, 2015.
[13] P. Karimi, “Electron beam melting of Alloy 718-Influence of process parameters on the microstructure,” no. 22. p. 65, 2018.
[14] D. Bürger, A. B. Parsa, M. Ramsperger, C. Körner, and G. Eggeler, “Creep properties of single crystal Ni-base superalloys (SX): A comparison between conventionally cast and additive manufactured CMSX-4 materials,” *Mater. Sci. Eng. A*, vol. 762, no. June, p. 138098, 2019.
[15] G. M. Peters, J. Hemptenmacher, J. Kumpfert[*] and C. Leyens DLR — German Aerospace Center, Cologne, “Structure and Properties of Titanium and Titanium alloys,” in *Titanium and Titanium Alloys: Fundamentals and Applications*, Christoph Leyens and Manfred Peters, Ed. 2003.
[16] S. Liu and Y. C. Shin, “Additive manufacturing of Ti6Al4V alloy: A review,” *Mater. Des.*, 2019.
[17] L. C. Zhang and Y. Liu, *Additive manufacturing of titanium alloys for biomedical applications*. Elsevier Inc., 2018.
[18] Arcam, “Ti6Al4V Titanium Alloy,” pp. 4–6, 1000.
[19] S. Tolvanen, “Welding of Ti-6Al-4V : Influence of welding process and alloy composition on microstructure and properties,” 2018.
[20] R. R. and K. R. Tadeusz Hryniewicz, “Magnetoelectropolished Titanium Biomaterial,” *Heavy Met. Remov. with Phytoremediation*, vol. i, no. tourism, p. 13, 2011.
[21] B. Sefer, *Oxidation and alpha-case phenomena in titanium alloys used in aerospace industry: Ti–6Al–2Sn–4Zr–2Mo and Ti–6Al–4V*. 2014.
[22] Matthew Donachie, *Titanium: A Technical Guide*, 2nd ed. ASM international, 2000.
[23] L. M. Gammon, R. D. Briggs, J. M. Packard, K. W. Batson, R. Boyer, and C. W. Domby, “Metallography and Microstructures of Titanium and Its Alloys,” vol. 9, 2004.
[24] J. Dutta Majumdar and I. Manna, *Laser surface engineering of titanium and its alloys for improved wear, corrosion and high-temperature oxidation resistance*. Elsevier Ltd., 2014.
[25] A. A. ANTONYSAMY, “Microstructure, Texture and Mechanical Property Evolution during Additive Manufacturing of Ti6Al4V Alloy for Aerospace Applications,” 2012.
[26] A. A. Antonysamy, J. Meyer, and P. B. Prangnell, “Effect of build geometry on the β-grain structure and texture in additive manufacture of Ti6Al4V by selective electron beam melting,” *Mater. Charact.*, vol. 84, pp. 153–168, 2013.

[27] R. Pederson, “Microstructure and Phase Transformation of Ti-6Al-4V,” 2002.
[28] G. E. Totten and D. S. Mackenzie, “Principles of Heat Treating of Nonferrous Alloys[1],” *Heat Treat. Nonferrous Alloy.*, vol. 4, pp. 3–31, 2016.
[29] B. Carreon, Hector & Ruiz, Alberto & Santoveña, “Study of Aging Effects in a Ti-6AL-4V Alloy with Widmanstatten and Equiaxed Microstructures by Non-Destructive Means,” 2014.
[30] H. Galarraga, D. A. Lados, R. R. Dehoff, M. M. Kirka, and P. Nandwana, “Effects of the microstructure and porosity on properties of Ti-6Al-4V ELI alloy fabricated by electron beam melting (EBM),” *Addit. Manuf.*, vol. 10, pp. 47–57, 2016.
[31] N. Pushilina *et al.*, “Influence of manufacturing parameters on microstructure and hydrogen sorption behavior of electron beam melted titanium Ti-6Al-4V alloy,” *Materials (Basel).*, vol. 11, no. 5, 2018.
[32] I. Katzarov, S. Malinov, and W. SHA, “Finite element modeling of morphology of beta to alpha phase transformation in Ti-6Al-4V Alloy,” *Metall. Mater. Trans. A*, vol. 33, no. 4, pp. 1027–1040, 2002.
[33] M. Jamshidinia, F. Kong, and R. Kovacevic, “ Numerical Modeling of Heat Distribution in the Electron Beam Melting ® of Ti-6Al-4V ,” *J. Manuf. Sci. Eng.*, vol. 135, no. 6, p. 061010, 2013.

Appendix 1: Specimen naming

Specimen naming scheme for the five different build plates with 8-16 specimens (cubes) each. Point distance, number of points, time for all spots, beam current, spot time, energy all points and volume energy for each specimen given according to the table.

Specimen name	Point distance [mm]	Number of point [#]	Time for all spots [s]	Current [mA]	Spot time [ms]	Energy all points [J]	Volume energy [J/mm3]
BV1.1	0,2	5625	2,25	**1,67**	0,4	225	**20**
BV1.2	0,2	5625	2,25	**2,17**	0,4	292,5	**26**
BV1.3	0,2	5625	2,25	**2,67**	0,4	360	**32**
BV1.4	0,2	5625	2,25	**3,17**	0,4	427,5	**38**
BV1.5	0,2	5625	2,25	**3,67**	0,4	495	**44**
BV1.6	0,2	5625	2,25	**4,17**	0,4	562,5	**50**
BV1.7	0,2	5625	2,25	**4,67**	0,4	630	**56**
BV1.8	0,2	5625	2,25	**5,17**	0,4	697,5	**62**
BV1.9	0,2	5625	2,25	**5,67**	0,4	765	**68**
BV1.10	0,2	5625	2,25	**6,17**	0,4	832,5	**74**
BV1.11	0,2	5625	2,25	**6,67**	0,4	900	**80**
BV1.12	0,2	5625	2,25	**7,17**	0,4	967,5	**86**
BV1.13	0,2	5625	2,25	**7,67**	0,4	1035	**92**
BV1.14	0,2	5625	2,25	**8,17**	0,4	1102,5	**98**
BV1.15	0,2	5625	2,25	**8,67**	0,4	1170	**104**
BV1.16	0,2	5625	2,25	**9,17**	0,4	1237,5	**110**
BV2.1	0,1	22500	2,25	**1,17**	0,1	157,5	**14**
BV2.2	0,1	22500	2,25	**1,67**	0,1	225	**20**
BV2.3	0,1	22500	2,25	**2,17**	0,1	292,5	**26**
BV2.4	0,1	22500	2,25	**2,67**	0,1	360	**32**
BV2.5	0,1	22500	2,25	**3,17**	0,1	427,5	**38**
BV2.6	0,1	22500	2,25	**3,67**	0,1	495	**44**
BV2.7	0,1	22500	2,25	**4,17**	0,1	562,5	**50**
BV2.8	0,1	22500	2,25	**4,67**	0,1	630	**56**
BV2.9	0,1	22500	2,25	**5,17**	0,1	697,5	**62**
BV2.10	0,1	22500	2,25	**5,67**	0,1	765	**68**
BV2.11	0,1	22500	2,25	**6,17**	0,1	832,5	**74**
BV2.12	0,1	22500	2,25	**6,67**	0,1	900	**80**
BV2.13	0,1	22500	2,25	**7,17**	0,1	967,5	**86**
BV2.14	0,1	22500	2,25	**7,67**	0,1	1035	**92**
BV2.15	0,1	22500	2,25	**8,17**	0,1	1102,5	**98**
BV2.16	0,1	22500	2,25	**8,67**	0,1	1170	**104**
BV3.1	0,5	900	2,25	**2,67**	2,5	360	**32**
BV3.2	0,5	900	2,25	**3,17**	2,5	427,5	**38**
BV3.3	0,5	900	2,25	**3,67**	2,5	495	**44**
BV3.4	0,5	900	2,25	**4,17**	2,5	562,5	**50**
BV3.5	0,5	900	2,25	**4,67**	2,5	630	**56**
BV3.6	0,5	900	2,25	**5,17**	2,5	697,5	**62**
BV3.7	0,5	900	2,25	**5,67**	2,5	765	**68**
BV3.8	0,5	900	2,25	**6,17**	2,5	832,5	**74**
BV3.9	0,5	900	2,25	**6,67**	2,5	900	**80**
BV3.10	0,5	900	2,25	**7,17**	2,5	967,5	**86**
BV3.11	0,5	900	2,25	**7,67**	2,5	1035	**92**
BV3.12	0,5	900	2,25	**8,17**	2,5	1102,5	**98**
BV3.13	0,5	900	2,25	**8,67**	2,5	1170	**104**
BV3.14	0,5	900	2,25	**9,17**	2,5	1237,5	**110**
BV3.15	0,5	900	2,25	**9,67**	2,5	1305	**116**
BV3.16	0,5	900	2,25	**10,17**	2,5	1372,5	**122**
BV4.1	0,3	2500	2,25	**2,17**	0,9	292,5	**26**
BV4.2	0,3	2500	2,25	**2,67**	0,9	360	**32**
BV4.3	0,3	2500	2,25	**3,17**	0,9	427,5	**38**
BV4.4	0,3	2500	2,25	**3,67**	0,9	495	**44**
BV4.5	0,3	2500	2,25	**4,17**	0,9	562,5	**50**
BV4.6	0,3	2500	2,25	**4,67**	0,9	630	**56**
BV4.7	0,3	2500	2,25	**5,17**	0,9	697,5	**62**
BV4.8	0,3	2500	2,25	**5,67**	0,9	765	**68**
BV4.9	0,3	2500	2,25	**6,17**	0,9	832,5	**74**
BV4.10	0,3	2500	2,25	**6,67**	0,9	900	**80**
BV4.11	0,3	2500	2,25	**7,17**	0,9	967,5	**86**
BV4.12	0,3	2500	2,25	**7,67**	0,9	1035	**92**
BV4.13	0,3	2500	2,25	**8,17**	0,9	1102,5	**98**
BV4.14	0,3	2500	2,25	**8,67**	0,9	1170	**104**
BV4.15	0,3	2500	2,25	**9,17**	0,9	1237,5	**110**
BV4.16	0,3	2500	2,25	**9,67**	0,9	1305	**116**

BV5.1	0,2	5625	1,41	**14**	0,25	1181,25	**105**
BV5.2	0,2	5625	1,41	**16**	0,25	1350	**120**
BV5.3	0,2	5625	1,41	**18**	0,25	1518,75	**135**
BV5.4	0,2	5625	1,41	**20**	0,25	1687,5	**150**
BV5.5	0,25	3600	0,9	**14**	0,25	756	**67,2**
BV5.6	0,25	3600	0,9	**16**	0,25	864	**76,8**
BV5.7	0,25	3600	0,9	**18**	0,25	972	**86,4**
BV5.8	0,25	3600	0,9	**20**	2,5	1080	**96**
BV5.9	0,5	900	2,25	**10,67**	2,5	1440	**128**
BV5.10	0,5	900	2,25	**11,17**	2,5	1507,5	**134**
BV5.11	0,5	900	2,25	**11,67**	2,5	1575	**140**
BV5.12	0,5	900	2,25	**12,17**	2,5	1642,5	**146**
BV5.13	0,5	900	2,25	**12,67**	2,5	1710	**152**
BV5.14	0,5	900	2,25	**13,17**	2,5	1777,5	**158**
BV5.15	0,5	900	0,36	**25**	0,4	540	**48**
BV5.16	0,5	900	0,45	**30**	0,5	810	**72**